# Single-Shot Reconstruction of Electron Beam Longitudinal Phase Space in a Laser Wakefield Accelerator

```
Y. Ma<sup>®</sup>, <sup>1,2,3,4,*</sup> M. J. V. Streeter<sup>®</sup>, <sup>2,3,5</sup> F. Albert, <sup>6</sup> N. Bourgeois, <sup>7</sup> S. Cipiccia<sup>®</sup>, <sup>8,9</sup> J. M. Cole<sup>®</sup>, <sup>10</sup> S. J. D. Dann<sup>®</sup>, <sup>2,3</sup> K. Falk, <sup>11,12,13</sup> E. Gerstmayr<sup>®</sup>, <sup>10,5</sup> I. Gallardo González<sup>®</sup>, <sup>14</sup> A. Higginbotham, <sup>15</sup> A. E. Hussein<sup>®</sup>, <sup>1</sup> D. A. Jaroszynski<sup>®</sup>, <sup>16</sup> A. S. Joglekar, <sup>17,4</sup> B. Kettle<sup>®</sup>, <sup>10</sup> K. Krushelnick<sup>®</sup>, <sup>1,4</sup> N. Lemos<sup>®</sup>, <sup>6</sup> N. C. Lopes, <sup>10,18</sup> C. Lumsden, <sup>15</sup> O. Lundh<sup>®</sup>, <sup>14</sup> S. P. D. Mangles<sup>®</sup>, <sup>10</sup> K. G. Miller<sup>®</sup>, <sup>19</sup> W. Mori, <sup>19</sup> Z. Najmudin<sup>®</sup>, <sup>10</sup> Q. Qian<sup>®</sup>, <sup>1</sup> P. P. Rajeev<sup>®</sup>, <sup>7</sup> D. Seipt<sup>®</sup>, <sup>1,2,3,20,21</sup> M. Shahzad, <sup>16</sup> M. Šmíd<sup>®</sup>, <sup>11</sup> R. Spesyvtsev, <sup>16</sup> D. R. Symes<sup>®</sup>, <sup>7</sup> G. Vieux, <sup>16</sup> L. Willingale<sup>®</sup>, <sup>1,2,3</sup> J. C. Wood<sup>®</sup>, <sup>10</sup> and A. G. R. Thomas<sup>®</sup>, <sup>1,2,3,4</sup>
                                        <sup>1</sup>Gérard Mourou Center for Ultrafast Optical Science, University of Michigan,
                                                                           Ann Arbor, Michigan 48109, USA
                                      <sup>2</sup>The Cockcroft Institute, Keckwick Lane, Daresbury, WA4 4AD, United Kingdom
                                      <sup>3</sup>Physics Department, Lancaster University, Lancaster LA1 4YB, United Kingdom
                                <sup>4</sup>Department of Nuclear Engineering and Radiological Sciences, University of Michigan,
                                                                           Ann Arbor, Michigan 48109, USA
                       <sup>5</sup>School of Mathematics and Physics, Queen's University Belfast, BT7 1NN Belfast, United Kingdom
                      <sup>6</sup>Lawrence Livermore National Laboratory (LLNL), P.O. Box 808, Livermore, California 94550, USA
                       <sup>7</sup>Central Laser Facility, STFC Rutherford Appleton Laboratory, Didcot OX11 0OX, United Kingdom
                               <sup>8</sup>Department of Medical Physics and Biomedical Engineering, University College London,
                                                                         London WC1E 6BT, United Kingdom
                                                 <sup>9</sup>Diamond Light Source, Harwell Science and Innovation Campus,
                                                             Fermi Avenue, Didcot OX11 0DE, United Kingdom
                                        <sup>10</sup>The John Adams Institute for Accelerator Science, Imperial College London,
                                                                          London, SW7 2AZ, United Kingdom
                          <sup>11</sup>Helmholtz-Zentrum Dresden-Rossendorf, Bautzner Landstraße 400, 01328, Dresden, Germany
                                                      <sup>12</sup>Technische Universität Dresden, 01062, Dresden, Germany
                                     <sup>13</sup>Institute of Physics of the ASCR, Na Slovance 2, Prague 182 21, Czech Republic
                                      <sup>14</sup>Department of Physics, Lund University, P.O. Box 118, S-22100, Lund, Sweden
                     <sup>15</sup>York Plasma Institute, Department of Physics, University of York, York YO10 5DD, United Kingdom
                            <sup>16</sup>SUPA, Department of Physics, University of Strathclyde, Glasgow G4 0NG, United Kingdom
                                                           <sup>17</sup>Ergodic LLC, San Francisco, California 94117, USA
                                            <sup>18</sup>GoLP/Instituto de Plasmas e Fusão Nuclear, Instituto Superior Técnico,
                                                                            U.L., Lisboa 1049-001, Portugal
                     <sup>19</sup>Department of Physics and Astronomy, University of California, Los Angeles, California 90095, USA
                                                     <sup>20</sup>Helmholtz Institut Jena, Fröbelstieg 3, 07743 Jena, Germany
                     <sup>21</sup>GSI Helmholtzzentrum für Schwerionenforschung GmbH, Planckstrasse 1, 64291 Darmstadt, Germany
```

(Received 3 June 2025; accepted 22 July 2025; published 2 September 2025)

We report on a single-shot longitudinal phase-space reconstruction diagnostic for electron beams in a laser wakefield accelerator via the experimental observation of distinct periodic modulations in the angularly resolved spectra. Such modulated angular spectra arise as a result of the direct interaction between the ultrarelativistic electron beam and the laser driver in the presence of the wakefield. A constrained theoretical model for the coupled oscillator, assisted by a genetic algorithm, can recreate the experimental electron spectra and, thus, fully reconstructs the longitudinal phase-space distribution of the electron beam with a temporal resolution of approximately 1.3 fs. In particular, it reveals the slice energy spread of the electron beam, which is important to measure for applications such as x-ray free electron lasers. In our experiment, the root-mean-square *slice* energy spread retrieved is bounded at 9.9 MeV, corresponding to a 0.9%–3.0% relative spread, despite the overall GeV energy beam having approximately 100% relative energy spread.

DOI: 10.1103/sxqf-l6mp Subject Areas: Optics, Plasma Physics

\*Contact author: yongm@umich.edu †Contact author: agrt@umich.edu

Published by the American Physical Society under the terms of the Creative Commons Attribution 4.0 International license. Further distribution of this work must maintain attribution to the author(s) and the published article's title, journal citation, and DOI.

#### I. INTRODUCTION

Laser wakefield acceleration (LWFA) [1-3] has gained much attention in the past few years due to its capability for generating multi-GeV electron beams [4-11] and the potential TeV energy gain with proposed dephasingless laser wakefield acceleration concepts [12-14]. It is now entering a new stage [15] toward practical applications in various science frontiers such as TeV electron-positron colliders [16], compact x-ray free electron lasers (XFELs) [17-19], and strong field quantum electrodynamics [20,21], to name but a few. These applications require, generally, very high beam quality, in terms of (slice) energy spread, emittance, beam charge, shot-to-shot stability, dark current, and so on. For example, a high-gain XFEL requires a relative energy spread smaller than the characteristic FEL parameter [18]. Although the relative energy spread of a beam from LWFA is typically large, the slice energy spread can be sufficiently small [22,23]. The required overall low energy spread of the beam can be achieved with the dechirping techniques in plasma wakefields [23–26] and radio-frequency (rf) cavities [27]. To achieve high beam qualities, one has to precisely control the beam dynamics in LWFA, which, in turn, can be done only with detailed diagnostics of the electron beam and wakefield dynamics. However, this is still extremely difficult due to the highly nonlinear acceleration process and the submicrometer, subfemtosecond spatiotemporal diagnostic requirements.

Recently, Downer et al. [28] summarized extensively the techniques for diagnosing the electron beam properties and even the wakefield structures. For example, state-of-the-art diagnosis of the wakefield structures have been performed with frequency-domain holography [29–31], femtosecond shadowgraphy [32-35], Faraday rotation [36,37], and electron radiography [38-40]. The evolution of the wakefield has also been investigated with multiple-shot transverse shadowgraphy [32] and single-shot frequencydomain streak cameras [41]. The techniques of diagnosing electron beam charge and energy are rather mature nowadays, normally with calibrated scintillating screens or image plates together with magnetic spectrometers which also provide spatial resolving capability. Slice energy spread, an important parameter that determines the minimal achievable energy spread [18,42], has not been measured in LWFA directly, although indirect measurement with coherent transition radiation has been performed [22]. Transverse beam emittance has been measured directly with a destructive conventional pepper-pot mask [43,44] and focus scan technique [45] and indirectly with betatron [46-48] and Thomson scattering [49–51] x-ray spectroscopy. The temporal beam profile has been retrieved from the coherent transition radiation when passing through the plasmavacuum boundary [52,53] or a radiator [54-59], from the magneto-optic technique [37], and by the transverse deflection of a laser [60].

It is worth noting that the wakefield structures diagnosed so far provide little information on the electron beams. The techniques for electron beam characterization are normally designed very specifically for one particular property, and none of these techniques give insight on the phase-space distributions. Thus, the single-shot direct diagnosis of the electron beam in 6D phase space is still extremely challenging.

Here, we present a single-shot diagnosis of the electron beam's longitudinal and potentially a full phase-space distribution using a standard angularly resolved electron spectrum combined with a constrained theoretical model that describes the resulting, unique herringbonelike periodic modulations. Such modulated spectra are a result of the direct interaction between the electron beam and the laser pulse while inside the wakefield [61]. The theoretical model, which couples the motion of electrons in the laserdriven wakefields and the oscillations in the laser fields, successfully captures the unique features of the spectra and, hence, reconstructs the longitudinal phase-space distribution of the electron beams with a temporal resolution better than that of the state-of-the-art X-band transverse deflection structure [62] that are used predominately in conventional rf accelerators. Such reconstruction reveals in great detail the transverse and longitudinal momentum distributions, which give the energy chirp of the electron beam and bunch shape (and, hence, pulse duration) as well as slice energy spread.

### II. EXPERIMENT

The experiments were performed on the Gemini laser at the Central Laser Facility (United Kingdom). The experimental setup, as shown in Fig. 1, is typical for LWFA experiments [63–67]. A linearly polarized laser beam, with a peak amplitude of the normalized vector potential of  $a_0 = 1.3 \pm 0.1$ , a full width at half maximum (FWHM) pulse duration of  $52 \pm 4$  fs, and FWHM focal spot of

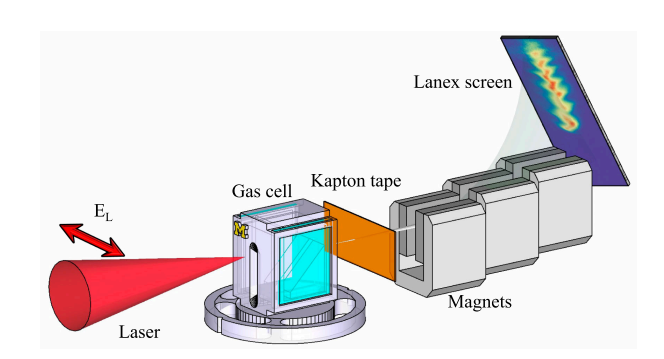


FIG. 1. Schematic of the experimental setup. A horizontally lineally polarized laser pulse was focused on the entrance of a two-stage gas cell. A thin Kapton tape was placed after the gas cell to block the residual laser pulse. The LWFA-generated electron beam was deflected by a permanent magnet in the vertical direction to resolve the energy spectrum.

 $50(\pm 2)~\mu m \times 40(\pm 2)~\mu m$ , was focused into a 3D-printed two-stage variable-length gas cell [66]. The first stage was filled with a gas mixture with 2% nitrogen and 98% helium as an "injector," and the second stage was filled with pure helium as the "accelerator" stage. The plasma density in the gas cells was varied in the range  $n_e = 0-2.6 \times 10^{18}~{\rm cm}^{-3}$ , measured with Raman sidescattering [63]. The angularly resolved electron spectrum was measured by an electron spectrometer, which consists of permanent magnets with measured magnetic field distribution and Lanex screens. The laser polarization is perpendicular to the magnetic deflection, so that the modulation of the spectrum due to the laser can be resolved on the detector.

Typical angular spectra of the electron beams with obvious modulation are shown in Fig. 2(a). Unlike the ordinary energy spectra, which can be found in Refs. [64–67] for the same experimental campaign, these reported here show extraordinary transverse oscillations, i.e., a "herringbone" structure. For all of them, the upper and the lower part of the oscillation crests (the peaks and valleys) are always offset. This can be explained only by the fact that the transverse momentum modulation was caused by the laser field.

The modulated electron spectra reveal the temporal beam profile and, hence, the pulse duration, as well as the centroids of the transverse and longitudinal momenta

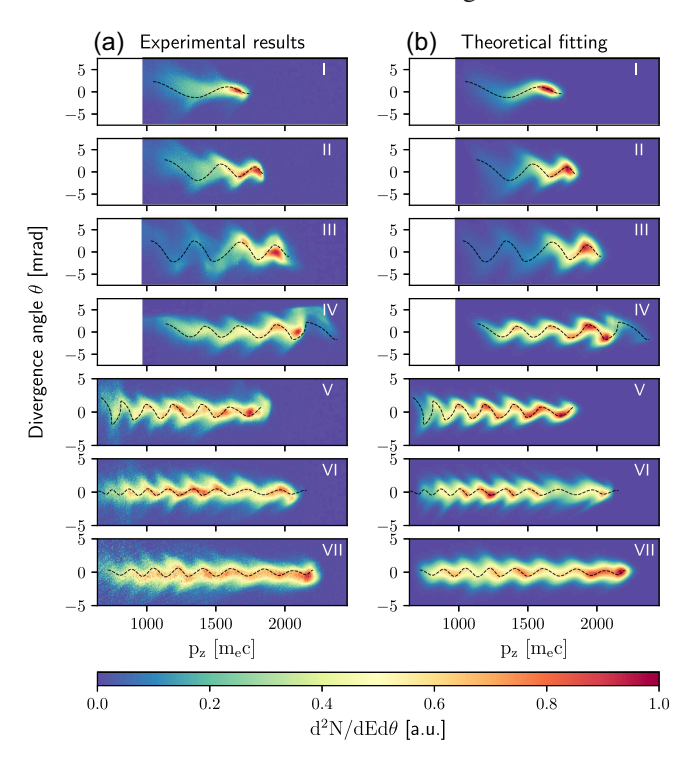


FIG. 2. Herringbone structures observed in (a) experiment and (b) the corresponding theoretical fittings. For each row, the identical black dashed lines represent the centroids of the theoretical fit. Note that the experimental data here are selected to show different numbers of laser cycles. The different energy ranges between I–IV and V–VII are due to different electron spectrometer configurations.

distributions. With these three aspects as inputs, we reconstructed the electron spectra, as shown in Fig. 2(b), based on the theoretical model in Sec. III and the method explained in Sec. III A. As can be seen from the comparison between Figs. 2(a) and 2(b), the reconstructed spectra agree with the experimental results quantitatively well. This, on one hand, verifies the validation of the theoretical model; on the other hand, the comparison indicates that more information of the electron beam can be revealed with fitting parameters which are shown later.

### III. COUPLED MOTION OF ELECTRONS IN LASER-DRIVEN WAKEFIELDS AND LASER FIELDS

In this section, we give the details of the theoretical model and the method of electron spectrum reconstruction.

We first review the coupled motion of electrons undergoing betatron oscillations in laser-driven wakefields along with oscillations in the laser fields while including the accelerating fields of the wake. The interaction of the laser with electrons in the presence of plasma channel fields is a well-established area of research [68–75], which was often referred as direct laser acceleration. The difference here compared to typical studies is that the electron beam is ultrarelativistic when it starts to interact with the fields. In particular, this leads to the interaction being sensitive to the difference between the laser phase velocity and the electron beam velocity.

We establish a simple model with the following assumptions. Throughout, we use a system of normalized units with  $t \to \omega_p t$ ,  $\mathbf{x} \to \omega_p \mathbf{x}/c$ ,  $\mathbf{p} \to \mathbf{p}/m_e c$ ,  $\mathbf{A} \to e\mathbf{A}/m_e c$ , etc., with  $\omega_p = e\sqrt{n_0/m_e}\varepsilon_0$  the plasma frequency corresponding to a reference plasma number density  $n_0$ . A laser pulse with central wave number  $k_0$  propagates in the  $x_{\parallel}$ direction with group velocity  $v_q$  described by a transverse vector potential  $\mathbf{A}_{\perp}(\xi, \mathbf{x}_{\perp}, t)$  only (i.e., ignoring longitudinal field contributions), where the coordinates ( $\mathbf{x}_{\perp}, \xi =$  $x_{\parallel} - v_q t, t$ ) arise from a Galilean transform to a frame moving at  $v_q$  and  $\mathbf{x}_{\perp}$  is the position vector transverse to the wake propagation direction, e.g., in the x-y plane if  $x_{\parallel} \equiv z$ . A paraxial description of a pulsed laser typically leads to the ordering of gradient scales  $|k_0 \mathbf{A}_{\perp}| \gg |\partial \mathbf{A}_{\perp}/\partial x_{\perp}|$ ,  $|\partial \mathbf{A}_{\perp}/\partial \xi| \gg |\partial \mathbf{A}_{\perp}/\partial t|$ . For simplicity, we neglect the explicit *t* dependence, e.g., diffraction and focusing effects. Hence, we may write  $\mathbf{A}_{\perp} = \frac{1}{2}\tilde{\mathbf{A}}_{\perp}e^{ik_0\zeta} + \text{c.c.}$ , where the complex amplitude is  $\tilde{\mathbf{A}}_{\perp}(\xi,\mathbf{x}_{\perp})$  and the laser carrier phase depends on  $\zeta(\xi, t) \equiv x_{\parallel}(\xi, t) - v_{\phi}t$ , with  $v_{\phi}$  the laser phase velocity. The wake is generated by the laser ponderomotive force and, therefore, is also assumed to be a function of  $\xi$  and  $\mathbf{x}_{\perp}$  only and described by a wake potential  $\psi(\xi, \mathbf{x}_{\perp}) = \phi - v_{o}A_{\parallel}.$ 

It can be shown (see the Appendix) that, for an electron interacting with transverse laser fields in the presence of a

wake potential, the longitudinal momentum can be related to the transverse displacement  $\mathbf{x}_\perp$  and transverse momentum  $\mathbf{p}_\perp$  via

$$p_{\parallel} \simeq p_{\parallel 0} - \frac{\gamma_p^2}{p_{\parallel 0}} \left( \frac{1}{2} \alpha^2 p_{\parallel 0} \mathbf{x}_{\perp}^2 \pm \mathbf{p}_{\perp}^2 \right),$$
 (1)

where the  $\mathbf{x}_{\perp}^2$  term is due to betatron oscillations in the wakefield, linearized about the center with gradient  $\alpha^2$ , and the  $\mathbf{p}_{\perp}^2$  term is due to the oscillation in the laser fields. The term  $p_{\parallel 0}$  is the momentum of the particle in the wake in the absence of any transverse oscillations, because the contribution of the oscillations can be treated perturbatively under the conditions studied here. The " $\pm$ " sign depends on whether the particle is either faster or slower than the wake.

The transverse motion of the electrons obey solutions to a (damped) forced harmonic oscillator equation, as shown in the Appendix:

$$\mathbf{x}_{\perp} = \frac{\hat{\mathbf{e}}a_0}{k_0\eta\mathcal{Z}}\sin\left(k_0\zeta + \Phi\right) + \mathbf{x}_{\perp t},$$

$$\mathbf{p}_{\perp} = \frac{\hat{\mathbf{e}}a_0}{\mathcal{Z}}\cos\left(k_0\zeta + \Phi\right) + \mathbf{p}_{\perp t},$$
(2)

where the function  $\eta(\zeta, \mathbf{x}_{\perp}, t) = \gamma(v_{\parallel} - v_{\phi})$  describes the change in laser phase of the electron,  $\Phi$  is a constant phase term,  $\hat{\mathbf{e}}$  the polarization vector,  $a_0$  the peak amplitude of the normalized laser vector potential, and  $\mathcal{Z} = 1 - (\alpha^2 \gamma / 2k_0^2 \eta^2)$  describes a betatron resonance [69,76,77].  $\mathbf{x}_{\perp t}$  and  $\mathbf{p}_{\perp t}$  are the transient solutions to the oscillator equation and correspond to the betatron oscillations of the electrons in the wake in the absence of the laser. Together, Eqs. (1) and (2) describe the distinctive herringbone-shaped trajectory (see Fig. 10 in the Appendix).

## A. Reconstruction of the electron spectra and the retrieval of the phase space

In the presence of the laser and the wakefield, each trapped, high-energy electron should follow a trajectory given by Eqs. (1) and (2). At the end of the gas cell, the plasma is rapidly (with respect to  $\zeta$ ) switched off, and the canonical momentum is subsequently conserved so that the momentum distribution measured on the detector represents the particle phase space at the end of the plasma. To reconstruct the expected measured momentum distribution of the particles, we make an ergodic argument that the average behavior of electrons may be determined by assuming the electrons fill the trajectory of a single particle. However, the electrons will be on different trajectories owing to their initial energy spread or transverse momentum spread, etc. The magnetic spectrometer detector projects the distribution onto a 2D plane, and so, from here on, we specify the parallel and perpendicular directions to be labeled z and x, respectively. In the experiment here, x is in the laser polarization direction. The goal for matching experimental data, e.g., Fig. 3(a), is to find the distribution in phase space  $f(p_z, p_x; \zeta)$  constrained to be constructed only by trajectories that obey Eqs. (1) and (2). We note that the transient solution will be set by the initial betatron oscillations, which can be assumed to be adiabatically matched such that  $p_{xt}$  can be sampled from an assumed normal distribution with width  $\sigma_{p_x}$ .

The amplitude of the steady-state solution of Eq. (2) can be extracted from the envelope of the experimental spectrum from the herringbone, and that of the transient solution can be extracted from the width of the experimental spectrum. Thus, the transverse momentum can be rewritten as

$$p_x(\zeta) = \hat{p}_{xs}(\zeta) \frac{a_0}{\mathcal{Z}} \cos(k_0 \zeta + \Phi) + \hat{p}_{xt}(\zeta) p_{xt}.$$
 (3)

Here,  $\hat{p}_{xs}$  and  $\hat{p}_{xt}$  are the normalized envelope of the steady-state and transient transverse momentum distributions [as functions of  $p_z$  and, hence,  $\zeta$ , since  $p_z(\zeta)$  can be inferred from the observed oscillations] extracted from the experimental spectrum.  $a_0$  represents the momentum amplitude of the steady-state oscillation of each particle.  $p_{xt}$  represents the transient solution due to the betatron oscillation, which, therefore, takes the form of a normal distribution for a beam which can be characterized as  $p_{xt} = \sigma_{p_{xt}} \cdot \mathcal{N}$ , with its mean at 0 and the standard deviation as  $\sigma_{p_{xt}}$ ;  $\mathcal{N}$  stands for the standard normal distribution function. Similarly for the real-space distribution  $x(\zeta)$ .

Therefore, the longitudinal momentum distribution can be rewritten as

$$p_{z} = p_{z0} - \frac{\gamma_{p}^{2}}{p_{z0}} \left[ \frac{1}{2} \alpha^{2} p_{z0} \left( \frac{\hat{x}_{s} a_{0}}{k_{0} \eta \mathcal{Z}} \sin(k_{0} \zeta + \Phi) + \hat{x}_{t} \sigma_{x_{t}} \mathcal{N} \right)^{2} + \left( \frac{\hat{p}_{xs} a_{0}}{\mathcal{Z}} \cos(k_{0} \zeta + \Phi) + \hat{p}_{xt} \sigma_{p_{xt}} \mathcal{N} \right)^{2} \right]. \tag{4}$$

Here, we take the "+" sign in the parentheses in Eq. (1) for the reason explained in the Appendix. The first term on the right-hand side that is due to the wakefield acceleration takes the form  $p_{z0}=p_{z,\rm exp}+\Delta p_z$ , where  $p_{z,\rm exp}$  is the centroid that can be extracted from the experimental spectrum as we mentioned above and  $\Delta p_z=\sigma_{\Delta p_z}\cdot\mathcal{N}$  is due to the slice energy spread distribution. Note that we treat the slice energy spread  $\Delta E$  equivalent to the slice longitudinal momentum spread  $\Delta p_z$  as  $\Delta E\simeq \Delta p_z c$  for ultrarelativistic electrons.

Apart from the extracted transverse, longitudinal momentum distributions, and longitudinal beam profile as the backbone of the reconstruction, the unknown parameters  $\gamma_p$ ,  $\alpha$ ,  $a_0$ ,  $\sigma_{p_{xt}}$ ,  $\sigma_{x_t}$ ,  $\Phi$ , and  $\sigma_{\Delta p_z}$  serve as fitting parameters.

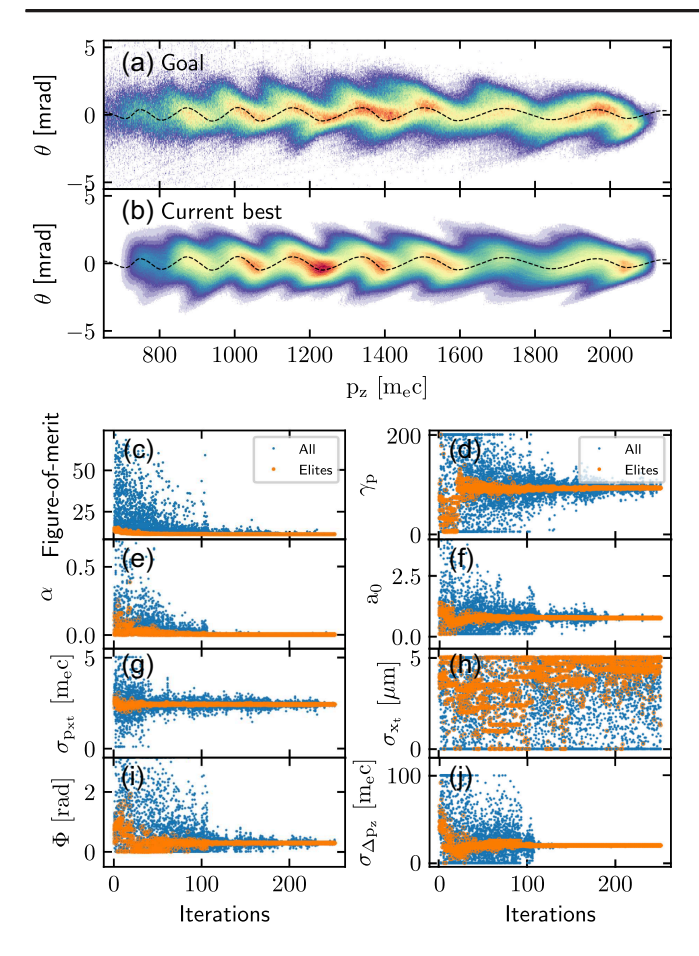


FIG. 3. Reconstruction optimization assisted with a differential genetic algorithm. (a) The experimental energy spectrum as the goal of the optimization. (b) The best reconstruction in the last iteration. The black dashed lines represent the centroid of the theoretical fitting, which was also displayed in (a) for reference. (c) The progression of the FOM. (d)–(j) The progression of all the genes, including (d)  $\gamma_p$ , (e)  $\alpha$ , (f)  $a_0$ , (g)  $\sigma_{p_{xt}}$ , (h)  $\sigma_{x_t}$ , (i)  $\Phi$ , and (j)  $\sigma_{\Delta_{p_z}}$ . In (c)–(j), blue dots represent all individuals, and the orange dots represent the best five in each iteration.

Therefore, the reconstruction is an optimization problem in a seven-dimensional parameter space that can be solved with a genetic algorithm (GA) [78-81]. Figure 3 demonstrates an example of the reconstruction optimization using the GA with a differential driver [78]. The goal for the GA was set as the experimental spectrum shown in Fig. 3(a). In each iteration, 20 individuals formed the parent generation, and five of the best ones were selected as the parents to pass their genes on to the next generation with a population of 20. For each individual, the spectrum was reconstructed by using Eqs. (3) and (4) with the fixed transverse, longitudinal and beam profile, and the seven parameters with random values as genes. Then, the randomly reconstructed spectrum was compared with the goal by using a figure-of-merit (FOM) function as the sum of the mean square error. The smaller the FOM, the better the GA performance. The five best children were selected as the new parents with a mutation and crossover of their genes to produce the next generation. The process repeated until the GA was converged.

The best reconstructed spectrum in the last iteration, as shown in Fig. 3(b), agrees quantitatively with the experimental spectrum in Fig. 3(a). Figure 3(c) shows the progression of the FOM, which clearly illustrates the convergence of the GA as the minimum of the FOM has stabilized. The convergence of all other parameters have meaningful physical implications. For example,  $\gamma_p$  depends on only the plasma density, and, due to the uniform plasma density distribution, it was found to be confined to approximately 100.  $\alpha$  reached a value close to 0, which indicates the disappearance of the plasma wake. The standard deviation of  $\Phi$  was found to be approximately zero, meaning that all particles are in phase (with the laser pulse) with a small phase error. It is worth noting that  $\sigma_{x_i}$ , which characterizes the particles' distribution in real space, did not converge due to the fact that  $\alpha$  converged to zero and the two parameters are coupled in Eq. (4). Note that the uniqueness of the GA solution was tested by performing hundreds of repeated GA runs with random starting points, which all converged to the same genes (except for  $\sigma_{x_i}$ ).

We now examine what information of the electron beam can be retrieved. The modulated electron energy spectra reveal three aspects directly: First, identifying the energy (and, hence, the longitudinal momentum) of each peak and valley, along with the assumption that they are separated by a half laser period in the time domain, the longitudinal momentum distribution  $p_{z,exp}(\zeta)$  is determined [black dashed line in Fig. 4(d)]; second, integrating the signals in between each peak and valley, the temporal beam profile and, hence, the pulse duration is determined [Fig. 4(b)] with a temporal resolution of a half laser period; third, the envelope of the angular spectrum gives the transverse momentum distribution  $p_{xs}(\zeta)$  [red dashed line in Fig. 4(c)]. With all the best-fitting parameters as well as the beam profile, the distributions of the transverse and longitudinal momenta can be given, as can be seen from the false color plots in Figs. 4(c) and 4(d). From Fig. 4(d), the distributions of the slice energy spread can be read out directly, as shown in Fig. 4(e). Apparently, the modulation due to the coupled motion increases the slice energy spread only with the minimum limited to the slice energy spread when modulations are absent. For this particular example, the slice energy spread is around  $\sigma_{\Delta p_z} \simeq 19.3 m_e c$ , corresponding to a relative energy spread of 0.9%-3.0%. Note that, while the slice energy spread can be a function of  $\zeta$ , the fact that a fixed single value can give a fitting close to the experimental spectrum indicates the weak dependence of slice energy spread on  $\zeta$ . Moreover, it is well known that the finite divergence angle of the electron beam causes an energy uncertainty on the electron spectrometer, which further smears the herringbone features. This indicates that

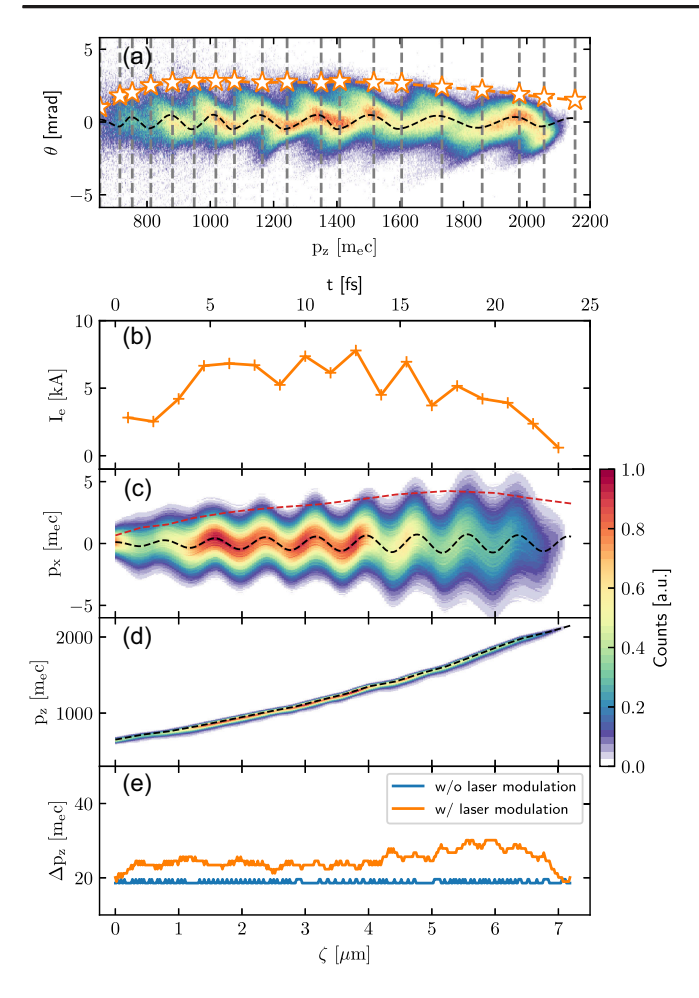


FIG. 4. Retrieval of the electron beam phase-space distributions for the same experimental spectra in Fig. 3(a). (a) The angularly resolved energy spectrum as an example to demonstrate the reconstruction of the temporal beam profile as well as the longitudinal and transverse momentum distributions. (b) Temporal beam profile. (c) Transverse momentum distribution. (d) Longitudinal momentum distribution. (e) Absolute slice energy spread with and without the modulation caused by the laser pulse.

the real slice energy spread could be even smaller, and the reconstruction gives an upper limit.

It is worth emphasizing the effects of the slice energy spread on the reconstruction. As demonstrated in Fig. 5, a small slice energy spread results in sharp edges, as in Fig. 5(a), while a large slice energy spread smears the herringbone features, as in Figs. 5(d) and 5(e). The case of  $\sigma_{\Delta p_z} = 20 m_e c$  [Fig. 5(c)] is close to the best fitting. Thus, our method provides a direct measurement of the slice energy spread. The diagnosis of the slice energy spread is of great importance in the design and the performance of XFELs [17,18,42], as it determines the lower limit on the projected energy spread. Also, FEL gain requires energy spread to be small only over the "cooperation length" in the undulators, which can be smaller than the electron beam

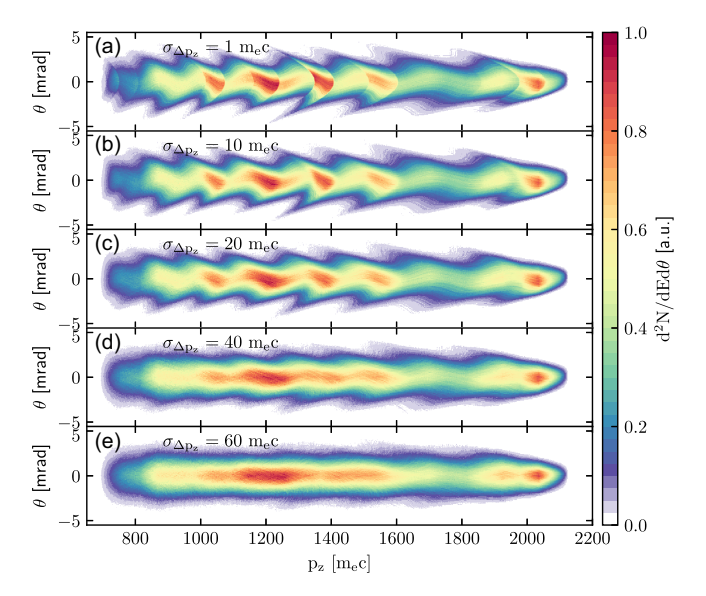


FIG. 5. Effect of slice energy spread on the reconstructed electron spectra. The absolute slice energy spreads in (a)–(e) are  $\sigma_{\Delta p_z} = 1, 10, 20, 40, 60 m_e c$ . All other fitting parameters are the same given by the optimization in Fig. 3.

length. Note that, although the method reported here relies on the energy chirp, monoenergetic electron beams can still be achieved with dechirping techniques [23–27].

#### **B.** Validation in particle-in-cell simulations

We demonstrate here the generation of herringbone in particle-in-cell (PIC) simulations and use the reconstruction of the herringbone to validate the method in Sec. III A.

The simulation was performed with the EPOCH 2D PIC code [82]. The simulation box with a moving window had dimensions of  $120 \times 300 \mu m$  in z and x with a resolution of  $\Delta z = 0.025 \ \mu \text{m}$  and  $\Delta x = 0.2 \ \mu \text{m}$ , where z and x are the longitudinal and transverse directions, respectively. There were eight macroparticles in each grid cell. The laser, with a wavelength of  $\lambda_L = 800$  nm, was linearly polarized in x with a peak amplitude of the normalized vector potential  $a_0 = 1.7$ , a FWHM pulse duration of  $\tau = 57$  fs, and a  $1/e^2$ spot size of  $w_0 = 40 \mu m$ . The laser pulse shape was Gaussian in both transverse and longitudinal directions. The background plasma was 32-mm-long preionized plasma with a uniform density of  $n_e = 5.5 \times 10^{17} \text{ cm}^{-3}$ . There was a 500-µm-long linear ramp at either end of the plasma region. The first 3 mm of the plasma region was doped with 2% preionized N<sup>5+</sup> ions to utilize ionization injection [83–88].

The simulation results are given in Figs. 6 and 7. Figure 6(a) shows a snapshot, at t = 110 ps, of the plasma density distribution overlapped with the density distribution of the injected electron beam and the laser field. At this moment, the electron beam has caught up with the rear of the laser pulse, which has caused the real-space  $(\zeta, x)$ 

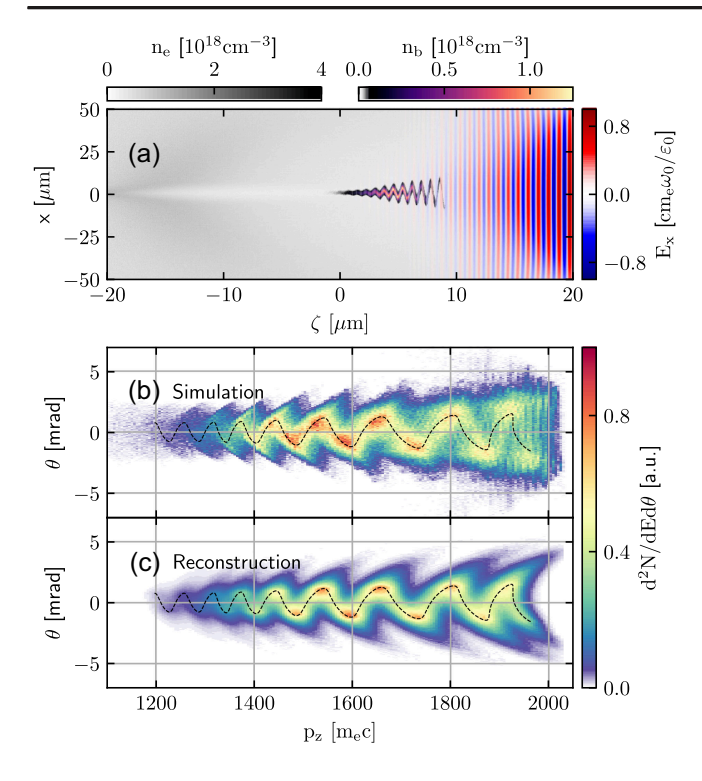


FIG. 6. Snapshot of the PIC simulation at t=110 ps. (a) Distributions of the plasma density  $n_e$ , accelerated electron bunch density  $n_b$ , and the transverse laser field  $E_x$ . (b) The modulated electron spectrum in the PIC simulation. (c) Reconstructed electron spectrum based on the theoretical model. The dashed curve in (c) is the centroid of the reconstructed spectrum which is also displayed in (b) for reference. The fitting parameters are  $\gamma_p=56.0$ ,  $\alpha=0.1$ ,  $a_0=3.0$ ,  $\sigma_{p_{xt}}=3.0m_e c$ ,  $\sigma_{x_t}=0.5~\mu m$ ,  $\Phi=\pi$ , and  $\sigma_{\Delta p_x}=16m_e c$ .

oscillation of the electron beam in phase with the laser. Because of the linear longitudinal accelerating field in the plasma wake and the fact that the electron bunch was injected locally, a quasilinear energy chirp developed naturally, as shown in Fig. 7(a). A monotonic energy chirp encodes the spatial modulation of the electron beam into its energy spectrum. As a result, collective oscillations emerge in the energy spectrum, as can be seen from Fig. 6(b). Such an oscillating spectrum is quite distinct from the sinusoidal collective betatron oscillation [89] or the angularly symmetric "scalloping" of electron beams [90,91] because of the fact that there is a phase shift of  $\pi$  between the top and the bottom halves of the spectrum and because the oscillations show a preferable bending direction in longitudinal. As mentioned above, the herringbone feature is a result of the coupled motion of electrons in the wakefield and the oscillations in the laser field, which can be described with the theoretical model. Therefore, we can reconstruct such modulated spectrum using the longitudinal and transverse momenta distributions extracted from the simulation. The reconstructed energy spectrum is illustrated in Fig. 6(c), with the centroid of distribution plotted

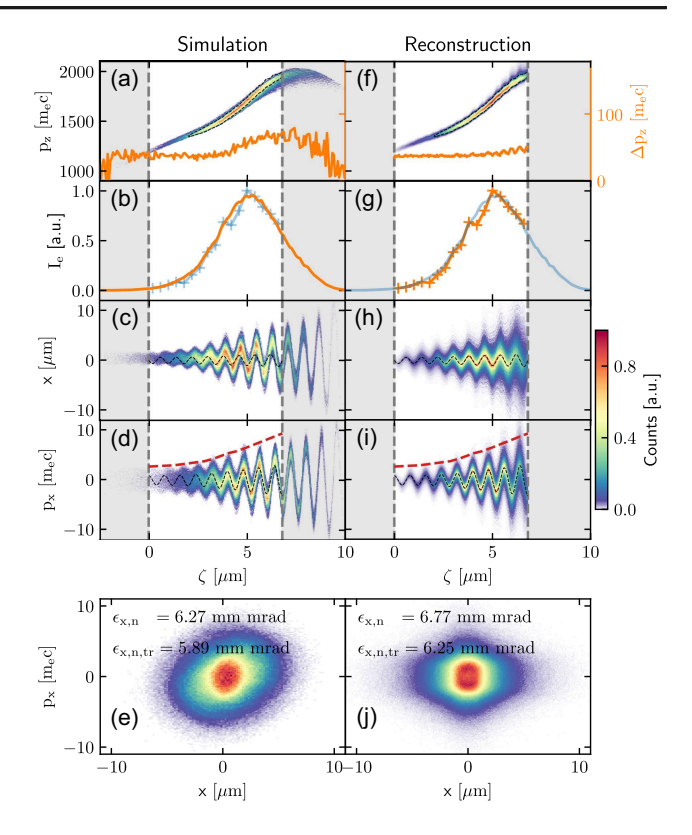


FIG. 7. Comparison between simulation results (left column) and the reconstruction (right column). (a),(f) Longitudinal momentum distributions  $(\zeta, p_z)$ . The orange curves are the slice energy spread distributions. (b),(g) Beam current distributions, i.e., temporal profiles. (c),(h) Real-space distributions ( $\zeta$ , x). (d), (i) Transverse momentum-space distributions  $(\zeta, p_x)$ . (e),(j) Transverse phase-space distributions  $(x, p_x)$ . The shaded areas in (a)-(i) are where no reconstruction can be made due to a low number of particles (on the left) and the flat chirp at the tip of the electron beam (on the right). Note that the dashed contour line in (f) represents the  $1/e^2$  intensity of the reconstruction. It was also displayed in (a) for reference. In both (b) and (g), the beam current from simulation and the reconstruction are overlapped for direct comparison. Similarly, in (c)–(i), the same dashed curves are overlapped on both simulation and reconstruction panels for comparison.

in both Figs. 6(b) and 6(c) for benchmarking. The reconstructed spectrum matches the simulated one very well. We emphasize that all the information used in the reconstruction process was entirely from the modulated electron spectrum in Fig. 6(b) and the method is the same as described in Sec. III A except for using the "–" sign in the parentheses in Eq. (1) for the reason explained in the Appendix.

The significance of performing the reconstruction using simulated data is that the retrieved phase-space distribution of the electron beam can be directly compared with the actual simulated data. Thus, we can examine the validation of the reconstruction method. For the example simulation in Fig. 6, the parameters for the optimal reconstruction are

 $\gamma_p=56.0,\, \alpha=0.1,\, a_0=3.0,\, \sigma_{p_{xt}}=3.0m_ec,\, \sigma_{x_t}=0.5$  µm,  $\Phi=\pi,\,$  and  $\sigma_{\Delta p_z}=16m_ec.$  With these fitting parameters, the reconstructed phase-space distributions are given in Figs. 7(f)–7(j). Figure 7(f) shows the reconstructed longitudinal phase space, which looks qualitatively similar to that from the simulation in Fig. 7(a). Quantitatively, the mean FWHM slice energy spread of the reconstructed longitudinal phase space is  $\bar{\Delta}p_{z,\text{rec}} = 46.0m_e c$ , compared to the actual value of  $\bar{\Delta}p_{z,\text{sim}} = 40.2m_ec$  in the simulation. Integrating the longitudinal phase-space distributions along the momentum dimension, we obtain the temporal beam profiles, as shown in Figs. 7(b) and 7(g), which show good agreement between the simulation and the reconstruction. The simulation gives a FWHM temporal pulse duration of  $\tau_{e, \text{sim}} = 12.06$  fs, while a Gaussian fitting of the reconstruction gives  $\tau_{e,rec} = 12.12$  fs, i.e., a relative error of 0.5%. It is worth mentioning that the part of the head and the tail of the beam cannot be reconstructed due to a low number of particles in the tail and the flat chirp at the head, as indicated by the shaded areas, which accounts for 17.6% of the total beam charge. Unlike the example given in Figs. 3 and 4, where only longitudinal phase space was retrieved, the fitting parameter  $\alpha \neq 0$  for the PIC simulation enables the retrieval of the transverse phasespace distribution. With a nonzero  $\alpha$ ,  $\sigma_{xt}$  can be determined, which leads to the reconstruction of the real-space distribution, as shown in Fig. 7(h). Together with the reconstructed transverse momentum distribution in Fig. 7(i), the transverse phase space can be retrieved, as shown in Fig. 7(i). The reconstructed transverse phase-space distribution looks similar to that of the simulation. Quantitatively, the normalized transverse emittance from the reconstruction is  $\epsilon_{x,n}(\epsilon_{x,n,\text{tr}}) = 6.77(6.25)$  mm mrad compared to 6.27 (5.89) mm mrad for the simulation, where  $\epsilon_{x,n}$  and  $\epsilon_{x,n,\text{tr}}$  are the normalized emittance and normalized trace-space emittance [92], respectively.

Note that the transverse phase-space distributions discussed here are modulated by the laser pulse. By subtracting the retrieved centroid trajectories [dashed curves in Figs. 7(h) and 7(i)], the transverse phase-space distribution can be decoupled from the laser modulations. In this case, the emittance is  $\epsilon_{x,n}(\epsilon_{x,n,\text{tr}}) = 5.26(4.94)$  mm mrad. In addition, such unmodulated transverse real-space and momentum-space distributions should be isotropic in transverse directions, governed by the random betatron motions. This means that the transverse phase-space distribution associated with the motion perpendicular to the laser polarization plane in  $(y, p_y)$  should be close to that in  $(x, p_x)$ . Therefore, the 6D phase-space distribution of the electron beam in the simulation is retrieved.

In addition to the retrieval of the electron properties, the reconstruction also reveals meaningful information about the wakefield. For example, among the seven fitting parameters,  $\gamma_p$  and  $\alpha$  are not directly related to the electron

beam properties but to the wakefield. With the fitted  $\gamma_p$ , one can infer the plasma density, since  $\gamma_p = \sqrt{n_c/n_p}$ . Here, the best-fitted  $\gamma_p = 56.0$  corresponds to a plasma density of  $n_e = 5.55 \times 10^{17}$  cm<sup>-3</sup>, which is in perfect agreement with the plasma density in the simulation. The parameter  $\alpha$ , which characterizes the strength of the wake potential, turns out to be much smaller than one ( $\alpha = 0.1$ ). This indicates a weak wakefield, which agrees with the density distribution in Fig. 6(a). However, it is worth noting that one should not take quantitatively the plasma density inferred from  $\gamma_p$ , the wake potential from  $\alpha$ , and the normalized laser intensity from  $a_0$  due to the rapid development of the plasma wave and the laser pulse.

The discrepancies between the simulation and reconstruction, such as the slight difference in emittance values and the difference of the fine features in the energy spectra, are probably due to numerical dispersion and to the inability to retrieve a portion of the beam.

#### IV. DISCUSSIONS

As mentioned above, Fig. 2(a) demonstrated the typical herringbone spectra as an example. The conditions under which the herringbone spectra were observed are summarized in Fig. 8. In the parameter space of plasma density and plasma length  $(n_p, L)$ , most of the herringbone spectra are

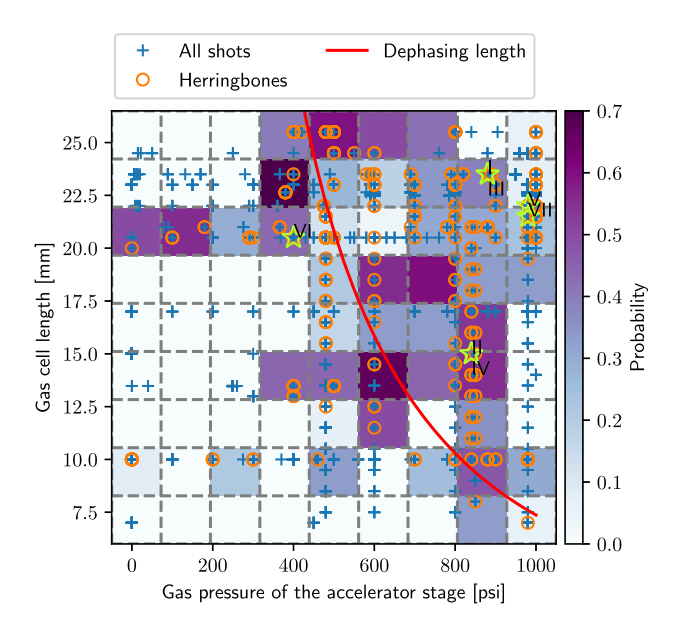


FIG. 8. Herringbone appearance in the parameter space of plasma density and plasma length. The blue plus signs represent the conditions for all shots, and the orange circles represent the conditions under which herringbone spectra were observed. Each data point represents multiple shots. The color represents the probability of the herringbone shots over the total shots in each separated region. The red curve indicates the dephasing length as a function of the plasma density using the scaling law from Ref. [93]. The stars represent the experimental shots in Fig. 2.

located in a belt near to the upper-right corner. This means the production of herringbone requires a relatively long plasma length and a high plasma density. Since the dephasing length depends on the plasma density as  $L_d=2/3(n_c/n_p)\lambda_p$  [93], we marked the dephasing length curve on the same parameter space  $(n_p,L)$ . It is clear that the majority of the herringbone spectra are very close to or above the dephasing length curve. This indicates that the electron beam must catch up with the laser pulse in the late stage of LWFA, ensuring the coupled motion of electrons in the wakefield and the laser pulse. Note that we also observed the spectra without herringbone structures throughout the whole parameter space, but at the optimal condition, i.e., beyond dephasing, the probability of the herringbone can be as high as 70%.

As mentioned in Sec. III B, the fitting parameters also reveal information about the wakefield and the laser pulse. The best-fitted  $\gamma_p$  lies in the range 20–100, which corresponds to the density range  $4.3 \times 10^{18}$ – $1.7 \times 10^{17}$ cm<sup>-3</sup>, and agrees with the measured density for the herringbone shots in Fig. 8. The wakefield strength parameter  $\alpha$  converged to zero indicates the disappearance of the wakefield, which agrees with the fact that the majority of the herringbone shots were observed beyond dephasing (as seen in Fig. 8).

The correlation between the longitudinal energy chirp and the electron beam charge could reveal the beam-loading effects in the plasma wake [94–98]. As shown in Fig. 9, the energy chirp varies quasilinearly as the

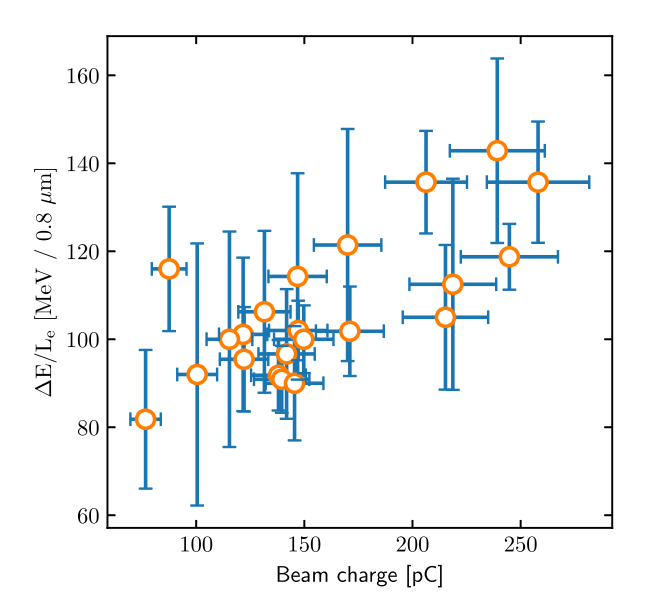


FIG. 9. Correlation between energy chirp and beam charge. The energy chirp was characterized by the average energy gradient, i.e., the energy difference between the bunch head and tail  $\Delta E$  over the total bunch length  $L_e$ . The horizontal error bars represent the uncertainty of the charge calibration. The vertical error bars represent the deviations to a linear chirp.

electron beam charge. This indicates the plasma wake was overloaded so that the injected electron beam flattens the longitudinal wakefield, which causes the head of the beam feels a stronger field than the tail and eventually leads to a positive energy chirp, as indicated by Fig. 7(a). Thus, the chirp direction can be determined.

The extracted transverse momentum distribution is imprinted with the amplitude of the laser pulse at the location of the electron beam, since  $p_{xs}(\zeta) \propto a_0(\zeta) m_e c$ . Hence, from the shape of  $p_{xs}(\zeta)$ , we can determine whether the electron beam is at the rear part of the laser pulse or whether it has passed through the peak of the pulse.

It is worth noting that we assume a flat laser phase in the reconstruction with a carrier wavelength of 800 nm. However, redshifting of the laser driver was observed in our experiment [63] with an average wavelength increase of approximately 20% for the herringbone shots recorded in this paper. This consequently places an uncertainty on the beam parameters, such as the temporal profile, but the slice energy spread retrieval is not affected, as reconstruction can be done with arbitrary  $\zeta$ . Redshifting occurs predominantly at the front of the pulse, so, in practice, the uncertainties are likely small, since the beam interacts with the back of the pulse.

#### V. CONCLUSION

In conclusion, we have applied a theoretical model describing the coupled motion of electrons in the laserdriven wakefields and the oscillations in the laser fields to reconstruct the electron longitudinal phase space in LWFA. Such coupled motion modulates the electron spectrum and results in unique herringbonelike structures. Our method is able to reconstruct the longitudinal momentum distribution, and, hence, the energy chirp, longitudinal spatial distribution, and the temporal beam shape as well as the pulse duration. Moreover, it reveals directly the slice energy spread of the electron beam in high resolution. It is worth mentioning that the full 6D phase space of the electron beam can be reconstructed with properly designed experimental scenarios, such as with a shaped laser pulse or a second laser pulse, where the electron spectral modulation happens inside the nonlinear plasma bubble. Such comprehensive diagnosis and reconstruction have been realized in a single-shot mode, which could advance the laser wakefield accelerator diagnostics for providing high-quality electron beams for various scientific frontiers.

Indeed, the theoretical model and the reconstruction method in our work are not constrained to the case of plasma accelerators. They can also be applied for electron beams from traditional accelerators, providing unprecedented temporal resolution, which could, therefore, substantially advance diagnostics for the whole accelerator community.

#### ACKNOWLEDGMENTS

This work was supported by the U.S. National Science Foundation under Grant No. 1804463, the United Kingdom STFC core Grants No. ST/P002056/1 (Cockcroft Institute) and No. ST/P000835/1 (John Adams Institute), and the United States Department of Energy Grants No. DE-NA0002372, No. DE-SC0022109, and No. DE-SC0016804. This work was partially supported by EuPRAXIA (Grant 653782), EC's LASERLAB-EUROPE No. 654148), United Kingdom EPSRC (Grants No. EP/ J018171/1, No. EP/J500094/1, and No. EP/N028694/1), Royal Society URF-R1221874, EuCARD-2 (Grant No. 312453), Swedish Research Council (VR 2019-04784, 2024-05698), the Knut and Alice Wallenberg Foundation (KAW 2019.0318, 2020.0111), the Extreme Light Infrastructure (ELI) European Project, Natural Science and Engineering Research Council of Canada, and FCT-Fundação para a Ciência e a Tecnologia, Ministério da Ciência e Ensino Superior, Portugal under Contract No. POCI/FIS/59574/2004 and by the auspices of the U.S. Department of Energy by Lawrence Livermore National Laboratory under Contract No. DE-AC52-07NA27344, as well as Lawrence Livermore National Security, LLC, and DOE Early Career Research Program No. SCW1575/1.

#### DATA AVAILABILITY

The data are not publicly available. The data are available from the authors upon reasonable request.

## APPENDIX: DETAILS OF THEORETICAL MODEL

After canonical transformation to the (wake) coordinates, the Hamiltonian for an electron in the combination of a laser and wake moving at  $v_q$  is

$$H = \sqrt{1 + [\mathbf{P} + \mathbf{A}(\xi, \mathbf{x}_{\perp}, t)]^2} - p_{\parallel} v_g - \psi(\mathbf{x}_{\perp}, \xi), \quad (A1)$$

where  ${\bf P}={\bf p}-{\bf A}$  is the canonical momentum and  ${\bf p}$  the kinetic momentum. The only explicit time dependence in this expression enters through the laser phase  $k_0\zeta(\xi,t)$ . We may write this expression as  $k_0\zeta(\xi,t)=k_0[\xi+(v_g-v_\phi)t]$ , which indicates that if  $v_g$  and  $v_\phi$  are assumed to be close to the speed of light, the explicit time dependence is small. Therefore, we may assume that H is approximately conserved such that

$$\gamma m_e - p_{\parallel} v_g - \psi \approx C_1, \tag{A2}$$

where  $\gamma = \sqrt{1 + [\mathbf{P} + \mathbf{A}(\mathbf{x}_{\perp}, \xi, t)]^2}$  and  $C_1$  is a constant of motion.

From the Hamiltonian, Eq. (A1), we may derive the equations of motion for the ith component of a test particle as

$$\frac{dP_i}{dt} = -e \frac{(\mathbf{P}_{\perp} + \mathbf{A}_{\perp})}{\gamma} \cdot \frac{\partial \mathbf{A}_{\perp}}{\partial x_i} - \frac{\partial \psi}{\partial x_i}.$$
 (A3)

For electrons that are close to the axis, it may be assumed that the transverse gradient in  $\mathbf{A}_{\perp}$  is negligible, so  $\mathbf{A}_{\perp}(\zeta,\mathbf{x}_{\perp})\simeq\mathbf{A}_{\perp}(\zeta)|_{\mathbf{x}_{\perp}=\mathbf{0}}$ . The plasma wake potential can be Taylor expanded in the transverse coordinates as

$$\psi = \psi_0(\xi) + \mathbf{x}_{\perp} \cdot \nabla_{\perp} \psi |_{\mathbf{x}_{\perp} = \mathbf{0}}(\xi)$$
$$+ \frac{1}{2} \mathbf{x}_{\perp} \mathbf{x}_{\perp} : \nabla_{\perp} \nabla_{\perp} \psi |_{\mathbf{x}_{\perp} = \mathbf{0}}(\xi) + \cdots, \qquad (A4)$$

where  $\nabla_{\perp}$  is the gradient in the plane perpendicular to the propagation direction and the colon: indicates the tensor product. For a wake with azimuthal symmetry, close to the axis the transverse gradient of the wake potential can, therefore, be written as  $\nabla_{\perp}\psi \simeq \mathbf{x}_{\perp}\nabla_{\perp}^{2}\psi|_{\mathbf{x}_{\perp}=\mathbf{0}}$ , which we define as  $-(\alpha^{2}/2)\mathbf{x}_{\perp}$ . In the "blowout" regime,  $\psi = [r_{b}(\xi)^{2}[1+\beta(\xi)]-r^{2}]/4$  [99] and so  $\alpha^{2}=1$ . For a partially evacuated wake, we may expect  $\alpha^{2}<1$ . The transverse equation of motion [Eq. (A3)] can, therefore, be written as

$$\frac{d}{dt}\left(\gamma \frac{d\mathbf{x}_{\perp}}{dt}\right) = -\frac{d\mathbf{A}_{\perp}}{dt} - \frac{\alpha^2}{2}\mathbf{x}_{\perp}.\tag{A5}$$

We may express this equation in terms of the laser phase coordinate,  $\zeta = x_{\parallel} - v_{\phi}t$ , by defining a function  $\eta(\zeta, \mathbf{x}_{\perp}, t) = \gamma(v_{\parallel} - v_{\phi})$  as

$$\frac{d}{d\zeta} \left( \eta \frac{d\mathbf{x}_{\perp}}{d\zeta} \right) = -\frac{d\mathbf{A}_{\perp}}{d\zeta} - \frac{\alpha^2 \gamma}{2\eta} \mathbf{x}_{\perp}. \tag{A6}$$

Note that  $\eta$  would be a constant of motion in vacuum (proportional to  $C_1$ ). Neglecting the transverse profile, the laser field is described by  $\mathbf{A}_{\perp} = \frac{1}{2}\tilde{\mathbf{A}}_{\perp}(\xi)\exp(ik_0\zeta) + \mathrm{c.c.}$ , and so Eq. (A6) can be written as

$$\left(\frac{d^2}{d\zeta^2} + 2\Gamma \frac{d}{d\zeta} + \kappa_{\beta}^2\right) \mathbf{x}_{\perp} = -\frac{e^{ik_0\zeta}}{2\eta} \left(ik_0\tilde{\mathbf{A}}_{\perp} + \frac{d\tilde{\mathbf{A}}_{\perp}}{d\zeta}\right) + \text{c.c.},$$
(A7)

where the betatron oscillation frequency (with respect to  $\zeta$ ) is  $\kappa_{\beta}=(\alpha/\eta)\sqrt{\gamma/2}$  and  $2\Gamma=d\eta/d\zeta$ . This is a driven oscillator equation, with  $\Gamma$  acting as a damping term. If we assume that the variation in  $\eta$  is slow compared with  $1/k_0$  and  $1/\kappa_{\beta}$  and the laser complex amplitude  $\tilde{\bf A}_{\perp}$  can be simply expressed in terms of an amplitude  $a_0$ , polarization vector  $\hat{\bf e}$ , and constant phase  $e^{i\Phi}$ ,  $\tilde{\bf A}_{\perp}=\hat{\bf e}a_0e^{i\Phi}$ , we have a standard driven oscillator equation with steady-state solutions

$$\mathbf{x}_{\perp s} = \frac{a_0 \hat{\mathbf{e}}}{k_0 \eta \mathcal{Z}} \sin(k_0 \zeta + \Phi), \qquad \mathbf{p}_{\perp s} = \frac{a_0 \hat{\mathbf{e}}}{\mathcal{Z}} \cos(k_0 \zeta + \Phi),$$
(A8)

where  $\mathcal{Z}=1-(\alpha^2\gamma/2k_0^2\eta^2)$  effectively describes the betatron resonance [69,76,77]. Note that, for an electron in vacuum and initially at rest,  $\alpha \to 0$  and  $\eta \to -1$ , thereby reducing Eq. (A8) to the expected solutions. Transient solutions to the equation are simply betatron oscillations with betatron frequency  $\kappa_\beta$ :

$$\mathbf{x}_{\perp t} = \mathbf{x}_1 \cos \kappa_{\beta} \zeta + \mathbf{x}_2 \sin \kappa_{\beta} \zeta, \tag{A9}$$

$$\mathbf{p}_{\perp t} = \mathbf{p}_1 \cos \kappa_{\beta} \zeta + \mathbf{p}_2 \sin \kappa_{\beta} \zeta. \tag{A10}$$

The general solutions are the superposition of the transient and steady-state solutions:

$$\mathbf{x}_{\perp} = \mathbf{x}_{\perp s} + \mathbf{x}_{\perp t},\tag{A11}$$

$$\mathbf{p}_{\perp} = \mathbf{p}_{\perp s} + \mathbf{p}_{\perp t}.\tag{A12}$$

The longitudinal momentum of the accelerated electron is given by rearranging Eq. (A2) [100]:

$$p_{\parallel} = \gamma_p^2 (C_1 + \psi) \left( v_p \pm \sqrt{1 - \frac{1 + \mathbf{p}_{\perp}^2}{\gamma_p^2 (C_1 + \psi)^2}} \right),$$
 (A13)

where  $\gamma_p = (1-v_p^2/c^2)^{-1/2}$  with  $v_p = v_g$  the phase velocity of the plasma wave. The two solutions given by the " $\pm$ " sign depend on whether the particle is faster or slower than  $v_p$ . The longitudinal momentum contains oscillations owing to both  $\mathbf{p}_{\perp}^2$  and  $\mathbf{x}_{\perp}^2$  through the (spatially dependent) wake potential  $\psi(\xi,\mathbf{x}_{\perp})$ . To the lowest order, the contribution from the  $\mathbf{p}_{\perp}^2$  oscillation term (assuming  $\psi$  is small, i.e., when the electron is close to maximum energy) is

$$\Delta p_{\parallel}(\mathbf{x}_{\perp} = \mathbf{0}) \simeq -\frac{\mathbf{p}_{\perp}^2}{2C_1},$$
 (A14)

and the contribution from the  $\boldsymbol{x}_{\perp}^2$  term is

$$\Delta p_{\parallel}(\mathbf{p}_{\perp} = \mathbf{0}) \simeq -\frac{1}{2}\alpha^2 \gamma_p^2 C_1 \mathbf{x}_{\perp}^2.$$
 (A15)

The relative ratio of the magnitude of these contributions is

$$\frac{|\Delta p_{\parallel}(\mathbf{x}_{\perp} = \mathbf{0})|}{|\Delta p_{\parallel}(\mathbf{p}_{\perp} = \mathbf{0})|} = \frac{k_0^2 \eta^2}{\gamma_p^2 C_1^2 \alpha^2}.$$
 (A16)

In general, the  $\eta$  function may be complex, and there could consequently be a resonant enhancement of the oscillations, making it difficult to predict the amplitude. However, since  $\mathbf{p}_{\perp}=ik_{0}\eta\mathbf{x}_{\perp}$  under the assumptions of the model, we may fit the expected distribution in  $p_{\parallel}$  using the measured  $\mathbf{p}_{\perp}$ . Expanding Eq. (A13) for  $p_{\perp}/p_{\parallel}\ll 1$ ,

$$p_{\parallel} \simeq p_{\parallel 0} - \frac{1}{2} \alpha^2 \gamma_p^2 \mathbf{x}_{\perp}^2 \mp \frac{\mathbf{p}_{\perp}^2}{2[C_1 + \psi_0(\xi)]}.$$
 (A17)

To leading order in  $\gamma_p$ ,  $p_{\parallel 0} \simeq 2\gamma_p^2 [C_1 + \psi_0(\xi)]$  is the momentum in the absence of oscillations, i.e., simply due to acceleration of an on-axis electron in the absence of a laser field, allowing Eq. (A17) to be rewritten as

$$p_{\parallel} \simeq p_{\parallel 0} - \frac{\gamma_p^2}{p_{\parallel 0}} \left( \frac{1}{2} \alpha^2 p_{\parallel 0} \mathbf{x}_{\perp}^2 \pm \mathbf{p}_{\perp}^2 \right).$$
 (A18)

Without considering the transient solution, i.e., for an electron initialized with zero transverse momentum, the typical trajectories can be seen in Fig. 10. With linear longitudinal acceleration, indicated by the black dotted line in Figs. 10(a) and 10(d), the shape of the trajectories in phase space  $(p_{\parallel}, p_{\perp}/p_{\parallel})$ , i.e., the angular spectrum in the case of a realistic electron bunch, is determined by the combination of  $a_0$ ,  $\alpha$ , and  $\gamma_p$ , as shown in Figs. 10(c) and 10(f). For some combinations, the oscillation patterns depart from a regular damping sinusoidal significantly, forming distinct herringbone features. The pointing direction of such features is determined by  $\alpha$  and  $\gamma_p$  through the sign change of  $\mathcal Z$  in Eq. (A8) as well as the choice of the sign in the parentheses in Eq. (A18).

For a realistic electron bunch, the central laser frequency  $k_0 \approx \omega_0$  can be substituted, and  $p_{\parallel 0}$  can be measured. The unknown parameters are those associated with the wakefield,  $\gamma_p$  and  $\alpha$ , which may be used as fitting parameters. The transient solutions due to betatron oscillations can be characterized with normal distributions. Note that  $\eta$  is not an independent parameter and can be determined by the electron energy  $\gamma$  and the phase velocity of the wakefield from  $\gamma_p$ . If the laser is assumed to have flat phase, the momentum as a function of laser phase  $\zeta$  can be determined, and, therefore, the momentum distribution in  $(\zeta, p_{\parallel 0})$  as well as  $(\zeta, \mathbf{p}_{\perp})$  space can be determined.

There are two important remarks to make. First, the significance of Eq. (A16) is that there is a  $\pi/2$  phase difference between the  $\mathbf{x}_{\perp}^2$  and  $\mathbf{p}_{\perp}^2$  contributions. Therefore, to observe a clear herringbone pattern in the electron spectrum, i.e., the  $(p_\parallel,\ p_\perp)$  phase space, the longitudinal momentum change needs to be dominated by the  $\mathbf{p}_{\perp}^2$  term. Otherwise, if the  $\mathbf{x}^2$  term dominates, individual trajectories with different amplitudes will smear the herringbone pattern due to the phase mismatch between  $p_{\perp}$  and  $p_{\parallel}$ . In other words, the wake potential parameter  $\alpha$  needs to be small to observe a clear herringbone pattern. This agrees with both the experimental and simulation results. Second, the choice of the sign in the parentheses in Eq. (A18) can be determined practically based on the measured electron spectrum. For example, when the hooks of the herringbone point to the high-energy end of the spectrum, for electrons on the same trajectory at the same  $p_{\parallel 0}$ , an increase in  $p_{\perp}$ 

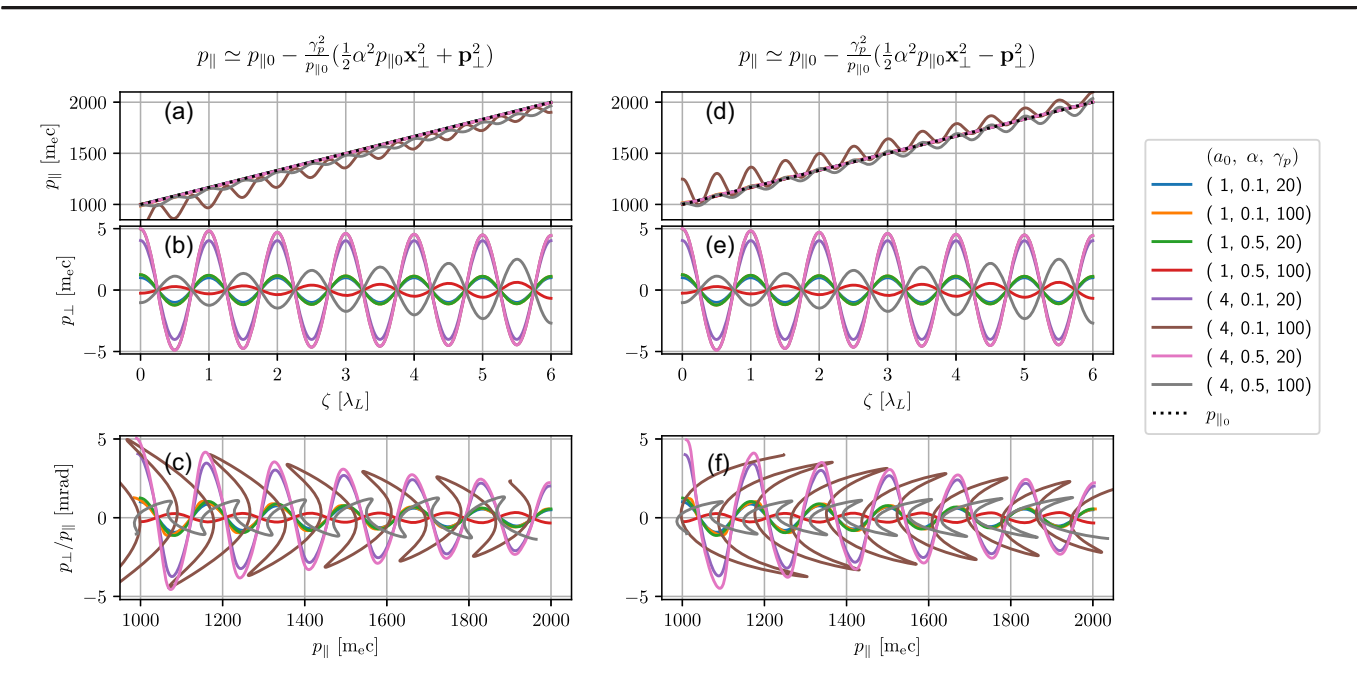


FIG. 10. Example trajectories of test particles for different  $a_0$ ,  $\alpha$ , and  $\gamma_p$ . The left and right columns are for the case of a positive and negative  $\mathbf{p}_{\perp}$  term, respectively, in Eq. (A18). (a),(d) Longitudinal momentum distributions. Black dotted lines represent the initial linear distributions. (b),(e) Transverse momentum distributions. (c),(f) Momentum distributions in  $(p_{\parallel}, p_{\perp})$ .

means an increase in  $p_{\parallel}$ . Thus, the contribution of the  $\mathbf{p}_{\perp}^2$  term is positive, and we take the "-" sign in the parentheses in Eq. (A18). This corresponds to the case of the experimental results. On the contrary, when the hooks point to the low-energy end of the spectrum, an increase in  $p_{\perp}$  means a decrease in  $p_{\parallel}$ . Thus, the contribution of the  $\mathbf{p}_{\perp}^2$  term is negative, and we take the "+" sign in the parentheses in Eq. (A18). This corresponds to the case of the simulation results. The fact that the hooks point to opposite directions in experiments and simulations might be an indication of numerical dispersion in PIC simulations. To eliminate the dispersion effect in plasma, one might perform such a reconstruction via direct laser-electron interaction in vacuum, similar to the proposed method in Ref. [101].

- [1] T. Tajima and J. M. Dawson, *Laser electron accelerator*, Phys. Rev. Lett. **43**, 267 (1979).
- [2] E. Esarey, C. B. Schroeder, and W. P. Leemans, *Physics of laser-driven plasma-based electron accelerators*, Rev. Mod. Phys. **81**, 1229 (2009).
- [3] V. Malka, Laser plasma accelerators, Phys. Plasmas 19, 055501 (2012).
- [4] A. Picksley, J. Stackhouse, C. Benedetti, K. Nakamura, H. E. Tsai, R. Li, B. Miao, J. E. Shrock, E. Rockafellow, H. M. Milchberg, C. B. Schroeder, J. van Tilborg, E. Esarey, C. G. R. Geddes, and A. J. Gonsalves, *Matched guiding and controlled injection in dark-current-free*, 10-GeV-class, channel-guided laser-plasma accelerators, Phys. Rev. Lett. 133, 255001 (2024).

- [5] C. Aniculaesei et al., The acceleration of a high-charge electron bunch to 10 geV in a 10-cm nanoparticle-assisted wakefield accelerator, Matter Radiat. Extremes 9, 014001 (2023).
- [6] A. J. Gonsalves et al., Petawatt laser guiding and electron beam acceleration to 8 GeV in a laser-heated capillary discharge waveguide, Phys. Rev. Lett. **122**, 084801 (2019).
- [7] B. Miao, J. E. Shrock, L. Feder, R. C. Hollinger, J. Morrison, R. Nedbailo, A. Picksley, H. Song, S. Wang, J. J. Rocca, and H. M. Milchberg, *Multi-GeV electron bunches from an all-optical laser wakefield accelerator*, Phys. Rev. X 12, 031038 (2022).
- [8] J. E. Shrock, E. Rockafellow, B. Miao, M. Le, R. C. Hollinger, S. Wang, A. J. Gonsalves, A. Picksley, J. J. Rocca, and H. M. Milchberg, Guided mode evolution and ionization injection in meter-scale multi-GeV laser wakefield accelerators, Phys. Rev. Lett. 133, 045002 (2024).
- [9] W. P. Leemans, A. J. Gonsalves, H.-S. Mao, K. Nakamura, C. Benedetti, C. B. Schroeder, C. Tóth, J. Daniels, D. E. Mittelberger, S. S. Bulanov, J.-L. Vay, C. G. R. Geddes, and E. Esarey, Multi-GeV electron beams from capillary-discharge-guided subpetawatt laser pulses in the self-trapping regime, Phys. Rev. Lett. 113, 245002 (2014).
- [10] X. Wang et al., Quasi-monoenergetic laser-plasma acceleration of electrons to 2 GeV, Nat. Commun. 4, 1988 (2013).
- [11] H. T. Kim, K. H. Pae, H. J. Cha, I. J. Kim, T. J. Yu, J. H. Sung, S. K. Lee, T. M. Jeong, and J. Lee, Enhancement of electron energy to the multi-GeV regime by a dual-stage laser-wakefield accelerator pumped by petawatt laser pulses, Phys. Rev. Lett. 111, 165002 (2013).

- [12] J. P. Palastro, J. L. Shaw, P. Franke, D. Ramsey, T. T. Simpson, and D. H. Froula, *Dephasingless laser wakefield acceleration*, Phys. Rev. Lett. **124**, 134802 (2020).
- [13] C. Caizergues, S. Smartsev, V. Malka, and C. Thaury, Phase-locked laser-wakefield electron acceleration, Nat. Photonics 14, 475 (2020).
- [14] A. Debus, R. Pausch, A. Huebl, K. Steiniger, R. Widera, T. E. Cowan, U. Schramm, and M. Bussmann, Circumventing the dephasing and depletion limits of laserwakefield acceleration, Phys. Rev. X 9, 031044 (2019).
- [15] F. Albert et al., 2020 roadmap on plasma accelerators, New J. Phys. 23, 031101 (2021).
- [16] W. Leemans and E. Esarey, Laser-driven plasma-wave electron accelerators, Phys. Today No. 62, 44 (2009).
- [17] C. Emma, J. Van Tilborg, R. Assmann, S. Barber, A. Cianchi, S. Corde, M. E. Couprie, R. D'Arcy, M. Ferrario, A. F. Habib et al., Free electron lasers driven by plasma accelerators: Status and near-term prospects, High Power Laser Sci. Eng. 9, e57 (2021).
- [18] W. Wang et al., Free-electron lasing at 27 nanometres based on a laser wakefield accelerator, Nature (London) **595**, 516 (2021).
- [19] M. Labat et al., Seeded free-electron laser driven by a compact laser plasma accelerator, Nat. Photonics 17, 150 (2022).
- [20] J.M. Cole et al., Experimental evidence of radiation reaction in the collision of a high-intensity laser pulse with a laser-wakefield accelerated electron beam, Phys. Rev. X 8, 011020 (2018).
- [21] K. Poder et al., Experimental signatures of the quantum nature of radiation reaction in the field of an ultraintense laser, Phys. Rev. X 8, 031004 (2018).
- [22] C. Lin, J. van Tilborg, K. Nakamura, A. J. Gonsalves, N. H. Matlis, T. Sokollik, S. Shiraishi, J. Osterhoff, C. Benedetti, C. B. Schroeder, C. Tóth, E. Esarey, and W. P. Leemans, Long-range persistence of femtosecond modulations on laser-plasma-accelerated electron beams, Phys. Rev. Lett. 108, 094801 (2012).
- [23] L. T. Ke, K. Feng, W. T. Wang, Z. Y. Qin, C. H. Yu, Y. Wu, Y. Chen, R. Qi, Z. J. Zhang, Y. Xu, X. J. Yang, Y. X. Leng, J. S. Liu, R. X. Li, and Z. Z. Xu, Near-GeV electron beams at a few per-mille level from a laser wakefield accelerator via density-tailored plasma, Phys. Rev. Lett. 126, 214801 (2021).
- [24] S. Jalas, M. Kirchen, P. Messner, P. Winkler, L. Hübner, J. Dirkwinkel, M. Schnepp, R. Lehe, and A. R. Maier, Bayesian optimization of a laser-plasma accelerator, Phys. Rev. Lett. 126, 104801 (2021).
- [25] Y. P. Wu, J. F. Hua, Z. Zhou, J. Zhang, S. Liu, B. Peng, Y. Fang, Z. Nie, X. N. Ning, C.-H. Pai, Y. C. Du, W. Lu, C. J. Zhang, W. B. Mori, and C. Joshi, *Phase space dynamics of a plasma wakefield dechirper for energy spread reduction*, Phys. Rev. Lett. 122, 204804 (2019).
- [26] A. Döpp, C. Thaury, E. Guillaume, F. Massimo, A. Lifschitz, I. Andriyash, J.-P. Goddet, A. Tazfi, K. Ta Phuoc, and V. Malka, *Energy-chirp compensation in a laser wakefield accelerator*, Phys. Rev. Lett. **121**, 074802 (2018).
- [27] P. Winkler et al., Active energy compression of a laser-plasma electron beam, Nature (London) 640, 907 (2025).

- [28] M. C. Downer, R. Zgadzaj, A. Debus, U. Schramm, and M. C. Kaluza, *Diagnostics for plasma-based electron accelerators*, Rev. Mod. Phys. 90, 035002 (2018).
- [29] N. H. Matlis, S. Reed, S. S. Bulanov, V. Chvykov, G. Kalintchenko, T. Matsuoka, P. Rousseau, V. Yanovsky, A. Maksimchuk, S. Kalmykov, G. Shvets, and M. C. Downer, Snapshots of laser wakefields, Nat. Phys. 2, 749 (2006).
- [30] P. Dong, S. A. Reed, S. A. Yi, S. Kalmykov, Z. Y. Li, G. Shvets, N. H. Matlis, C. McGuffey, S. S. Bulanov, V. Chvykov, G. Kalintchenko, K. Krushelnick, A. Maksimchuk, T. Matsuoka, A. G. R. Thomas, V. Yanovsky, and M. C. Downer, *Holographic visualization of laser wakefields*, New J. Phys. 12, 045016 (2010).
- [31] J. Cowley, C. Thornton, C. Arran, R. J. Shalloo, L. Corner, G. Cheung, C. D. Gregory, S. P. D. Mangles, N. H. Matlis, D. R. Symes, R. Walczak, and S. M. Hooker, *Excitation and control of plasma wakefields by multiple laser pulses*, Phys. Rev. Lett. 119, 044802 (2017).
- [32] A. Sävert, S. P. D. Mangles, M. Schnell, E. Siminos, J. M. Cole, M. Leier, M. Reuter, M. B. Schwab, M. Möller, K. Poder, O. Jäckel, G. G. Paulus, C. Spielmann, S. Skupin, Z. Najmudin, and M. C. Kaluza, *Direct observation of the injection dynamics of a laser wakefield accelerator using few-femtosecond shadowgraphy*, Phys. Rev. Lett. 115, 055002 (2015).
- [33] S. Kuschel, M. B. Schwab, M. Yeung, D. Hollatz, A. Seidel, W. Ziegler, A. Sävert, M. C. Kaluza, and M. Zepf, *Controlling the self-injection threshold in laser wakefield accelerators*, Phys. Rev. Lett. **121**, 154801 (2018).
- [34] M. F. Gilljohann, H. Ding, A. Döpp, J. Götzfried, S. Schindler, G. Schilling, S. Corde, A. Debus, T. Heinemann, B. Hidding, S. M. Hooker, A. Irman, O. Kononenko, T. Kurz, A. Martinez de la Ossa, U. Schramm, and S. Karsch, *Direct observation of plasma waves and dynamics induced by laser-accelerated electron beams*, Phys. Rev. X 9, 011046 (2019).
- [35] T. Kurz et al., Demonstration of a compact plasma accelerator powered by laser-accelerated electron beams, Nat. Commun. 12, 2895 (2021).
- [36] M. C. Kaluza, H.-P. Schlenvoigt, S. P. D. Mangles, A. G. R. Thomas, A. E. Dangor, H. Schwoerer, W. B. Mori, Z. Najmudin, and K. M. Krushelnick, *Measurement of magnetic-field structures in a laser-wakefield acceler-ator*, Phys. Rev. Lett. **105**, 115002 (2010).
- [37] A. Buck, M. Nicolai, K. Schmid, C. M. S. Sears, A. Sävert, J. M. Mikhailova, F. Krausz, M. C. Kaluza, and L. Veisz, Real-time observation of laser-driven electron acceleration, Nat. Phys. 7, 543 (2011).
- [38] Y. Wan, O. Seemann, S. Tata, I. A. Andriyash, S. Smartsev, E. Kroupp, and V. Malka, *Direct observation of relativistic broken plasma waves*. Nat. Phys. 18, 1186 (2022).
- [39] C. J. Zhang, J. F. Hua, Y. Wan, C.-H. Pai, B. Guo, J. Zhang, Y. Ma, F. Li, Y. P. Wu, H.-H. Chu, Y. Q. Gu, X. L. Xu, W. B. Mori, C. Joshi, J. Wang, and W. Lu, Femtosecond probing of plasma wakefields and observation of the plasma wake reversal using a relativistic electron bunch, Phys. Rev. Lett. 119, 064801 (2017).
- [40] C. J. Zhang, Y. Wan, B. Guo, J. F. Hua, C.-H. Pai, F. Li, J. Zhang, Y. Ma, Y. P. Wu, X. L. Xu, W. B. Mori, H.-H. Chu, J. Wang, W. Lu, and C. Joshi, *Probing plasma wakefields*

- using electron bunches generated from a laser wakefield accelerator, Plasma Phys. Controlled Fusion **60**, 044013 (2018).
- [41] Z. Li, H.-E. Tsai, X. Zhang, C.-H. Pai, Y.-Y. Chang, R. Zgadzaj, X. Wang, V. Khudik, G. Shvets, and M. C. Downer, Single-shot visualization of evolving laser wakefields using an all-optical streak camera, Phys. Rev. Lett. 113, 085001 (2014).
- [42] A. R. Maier, A. Meseck, S. Reiche, C. B. Schroeder, T. Seggebrock, and F. Grüner, *Demonstration scheme for a laser-plasma-driven free-electron laser*, Phys. Rev. X 2, 031019 (2012).
- [43] S. Fritzler, E. Lefebvre, V. Malka, F. Burgy, A. E. Dangor, K. Krushelnick, S. P. D. Mangles, Z. Najmudin, J.-P. Rousseau, and B. Walton, *Emittance measurements of a laser-wakefield-accelerated electron beam*, Phys. Rev. Lett. 92, 165006 (2004).
- [44] E. Brunetti, R. P. Shanks, G. G. Manahan, M. R. Islam, B. Ersfeld, M. P. Anania, S. Cipiccia, R. C. Issac, G. Raj, G. Vieux, G. H. Welsh, S. M. Wiggins, and D. A. Jaroszynski, Low emittance, high brilliance relativistic electron beams from a laser-plasma accelerator, Phys. Rev. Lett. 105, 215007 (2010).
- [45] S. K. Barber, J. van Tilborg, C. B. Schroeder, R. Lehe, H.-E. Tsai, K. K. Swanson, S. Steinke, K. Nakamura, C. G. R. Geddes, C. Benedetti, E. Esarey, and W. P. Leemans, *Measured emittance dependence on the injection method in laser plasma accelerators*, Phys. Rev. Lett. 119, 104801 (2017).
- [46] G. R. Plateau, C. G. R. Geddes, D. B. Thorn, M. Chen, C. Benedetti, E. Esarey, A. J. Gonsalves, N. H. Matlis, K. Nakamura, C. B. Schroeder, S. Shiraishi, T. Sokollik, J. van Tilborg, C. Toth, S. Trotsenko, T. S. Kim, M. Battaglia, T. Stöhlker, and W. P. Leemans, Low-emittance electron bunches from a laser-plasma accelerator measured using single-shot x-ray spectroscopy, Phys. Rev. Lett. 109, 064802 (2012).
- [47] S. Kneip et al., Characterization of transverse beam emittance of electrons from a laser-plasma wakefield accelerator in the bubble regime using betatron x-ray radiation, Phys. Rev. ST Accel. Beams 15, 021302 (2012).
- [48] A. Curcio, M. Anania, F. Bisesto, E. Chiadroni, A. Cianchi, M. Ferrario, F. Filippi, D. Giulietti, A. Marocchino, M. Petrarca, V. Shpakov, and A. Zigler, Trace-space reconstruction of low-emittance electron beams through betatron radiation in laser-plasma accelerators, Phys. Rev. Accel. Beams 20, 012801 (2017).
- [49] W. P. Leemans, R. W. Schoenlein, P. Volfbeyn, A. H. Chin, T. E. Glover, P. Balling, M. Zolotorev, K. J. Kim, S. Chattopadhyay, and C. V. Shank, X-ray based subpicosecond electron bunch characterization using 90° Thomson scattering, Phys. Rev. Lett. 77, 4182 (1996).
- [50] G. Golovin, S. Banerjee, C. Liu, S. Chen, J. Zhang, B. Zhao, P. Zhang, M. Veale, M. Wilson, P. Seller, and D. Umstadter, *Intrinsic beam emittance of laser-accelerated electrons measured by x-ray spectroscopic imaging*, Sci. Rep. 6, 24622 (2016).
- [51] J. M. Krämer, A. Jochmann, M. Budde, M. Bussmann, J. P. Couperus, T. E. Cowan, A. Debus, A. Köhler, M. Kuntzsch, A. Laso García, U. Lehnert, P. Michel,

- R. Pausch, O. Zarini, U. Schramm, and A. Irman, *Making spectral shape measurements in inverse compton scattering a tool for advanced diagnostic applications*, Sci. Rep. **8**, 1398 (2018).
- [52] W. P. Leemans, C. G. R. Geddes, J. Faure, C. Tóth, J. van Tilborg, C. B. Schroeder, E. Esarey, G. Fubiani, D. Auerbach, B. Marcelis, M. A. Carnahan, R. A. Kaindl, J. Byrd, and M. C. Martin, Observation of terahertz emission from a laser-plasma accelerated electron bunch crossing a plasma-vacuum boundary, Phys. Rev. Lett. 91, 074802 (2003).
- [53] J. van Tilborg, C. B. Schroeder, C. V. Filip, C. Tóth, C. G. R. Geddes, G. Fubiani, R. Huber, R. A. Kaindl, E. Esarey, and W. P. Leemans, *Temporal characterization of femtosecond laser-plasma-accelerated electron bunches using terahertz radiation*, Phys. Rev. Lett. 96, 014801 (2006).
- [54] Y. Glinec, J. Faure, A. Norlin, A. Pukhov, and V. Malka, Observation of fine structures in laser-driven electron beams using coherent transition radiation, Phys. Rev. Lett. 98, 194801 (2007).
- [55] A. D. Debus et al., Electron bunch length measurements from laser-accelerated electrons using single-shot thz time-domain interferometry, Phys. Rev. Lett. **104**, 084802 (2010).
- [56] O. Lundh, J. Lim, C. Rechatin, L. Ammoura, A. Ben-Ismaïl, X. Davoine, G. Gallot, J.-P. Goddet, E. Lefebvre, V. Malka, and J. Faure, Few femtosecond, few kiloampere electron bunch produced by a laser-plasma accelerator, Nat. Phys. 7, 219 (2011).
- [57] O. Lundh, C. Rechatin, J. Lim, V. Malka, and J. Faure, Experimental measurements of electron-bunch trains in a laser-plasma accelerator, Phys. Rev. Lett. **110**, 065005 (2013).
- [58] S. I. Bajlekov, M. Heigoldt, A. Popp, J. Wenz, K. Khrennikov, S. Karsch, and S. M. Hooker, Longitudinal electron bunch profile reconstruction by performing phase retrieval on coherent transition radiation spectra, Phys. Rev. ST Accel. Beams 16, 040701 (2013).
- [59] M. Heigoldt, A. Popp, K. Khrennikov, J. Wenz, S. W. Chou, S. Karsch, S. I. Bajlekov, S. M. Hooker, and B. Schmidt, *Temporal evolution of longitudinal bunch profile in a laser wakefield accelerator*, Phys. Rev. ST Accel. Beams 18, 121302 (2015).
- [60] C. J. Zhang, J. F. Hua, Y. Wan, B. Guo, C.-H. Pai, Y. P. Wu, F. Li, H.-H. Chu, Y. Q. Gu, W. B. Mori, C. Joshi, J. Wang, and W. Lu, Temporal characterization of ultrashort linearly chirped electron bunches generated from a laser wakefield accelerator, Phys. Rev. Accel. Beams 19, 062802 (2016).
- [61] K. Németh, B. Shen, Y. Li, H. Shang, R. Crowell, K. C. Harkay, and J. R. Cary, *Laser-driven coherent betatron oscillation in a laser-wakefield cavity*, Phys. Rev. Lett. **100**, 095002 (2008).
- [62] P. González Caminal et al., Beam-based commissioning of a novel x-band transverse deflection structure with variable polarization, Phys. Rev. Accel. Beams 27, 032801 (2024).
- [63] M. J. V. Streeter et al., Characterization of laser wakefield acceleration efficiency with octave spanning near-IR

- spectrum measurements, Phys. Rev. Accel. Beams 25, 101302 (2022).
- [64] A. Maitrallain et al., Parametric study of high-energy ringshaped electron beams from a laser wakefield accelerator, New J. Phys. 24, 013017 (2021).
- [65] B. Kettle *et al.*, Single-shot multi-keV x-ray absorption spectroscopy using an ultrashort laser-wakefield accelerator source, Phys. Rev. Lett. **123**, 254801 (2019).
- [66] A. E. Hussein et al., Laser-wakefield accelerators for highresolution x-ray imaging of complex microstructures, Sci. Rep. 9, 3249 (2019).
- [67] R. Spesyvtsev et al., Generation of electron high energy beams with a ring-like structure by a dual stage laser wakefield accelerator, in Relativistic Plasma Waves and Particle Beams as Coherent and Incoherent Radiation Sources III, edited by D. A. Jaroszynski and M. Hur, International Society for Optics and Photonics (SPIE, 2019), Vol. 11036, pp. 27–34.
- [68] A. Pukhov and J. Meyer-ter Vehn, Relativistic laserplasma interaction by multi-dimensional particle-in-cell simulations, Phys. Plasmas 5, 1880 (1998).
- [69] A. Pukhov, Z.-M. Sheng, and J. Meyer-ter Vehn, *Particle acceleration in relativistic laser channels*, Phys. Plasmas 6, 2847 (1999).
- [70] A. V. Arefiev, B. N. Breizman, M. Schollmeier, and V. N. Khudik, *Parametric amplification of laser-driven electron acceleration in underdense plasma*, Phys. Rev. Lett. 108, 145004 (2012).
- [71] A. P. L. Robinson, A. V. Arefiev, and D. Neely, Generating "superponderomotive" electrons due to a non-wake-field interaction between a laser pulse and a longitudinal electric field, Phys. Rev. Lett. 111, 065002 (2013).
- [72] X. Zhang, V. N. Khudik, and G. Shvets, *Synergistic laser-wakefield and direct-laser acceleration in the plasma-bubble regime*, Phys. Rev. Lett. **114**, 184801 (2015).
- [73] J.L. Shaw, N. Lemos, L.D. Amorim, N. Vafaei-Najafabadi, K. A. Marsh, F. S. Tsung, W. B. Mori, and C. Joshi, Role of direct laser acceleration of electrons in a laser wakefield accelerator with ionization injection, Phys. Rev. Lett. 118, 064801 (2017).
- [74] I. Gallardo González, H. Ekerfelt, M. Hansson, T. L. Audet, B. Aurand, F. G. Desforges, S. D. Dufrénoy, A. Persson, X. Davoine, C.-G. Wahlström, B. Cros, and O. Lundh, Effects of the dopant concentration in laser wakefield and direct laser acceleration of electrons, New J. Phys. 20, 053011 (2018).
- [75] T. Wang, V. Khudik, A. Arefiev, and G. Shvets, *Direct laser acceleration of electrons in the plasma bubble by tightly focused laser pulses*, Phys. Plasmas **26**, 083101 (2019).
- [76] C. Gahn, G. D. Tsakiris, A. Pukhov, J. Meyer-ter Vehn, G. Pretzler, P. Thirolf, D. Habs, and K. J. Witte, *Multi-meV electron beam generation by direct laser acceleration in high-density plasma channels*, Phys. Rev. Lett. 83, 4772 (1999).
- [77] S. P. D. Mangles, B. R. Walton, M. Tzoufras, Z. Najmudin, R. J. Clarke, A. E. Dangor, R. G. Evans, S. Fritzler, A. Gopal, C. Hernandez-Gomez, W. B. Mori, W. Rozmus, M. Tatarakis, A. G. R. Thomas, F. S. Tsung, M. S. Wei, and K. Krushelnick, *Electron acceleration in cavitated channels*

- formed by a petawatt laser in low-density plasma, Phys. Rev. Lett. **94**, 245001 (2005).
- [78] S.J.D. Dann et al., Laser wakefield acceleration with active feedback at 5 Hz, Phys. Rev. Accel. Beams 22, 041303 (2019).
- [79] J. Lin, Y. Ma, R. Schwartz, D. Woodbury, J. A. Nees, M. Mathis, A. G. R. Thomas, K. Krushelnick, and H. Milchberg, Adaptive control of laser-wakefield accelerators driven by mid-ir laser pulses, Opt. Express 27, 10912 (2019).
- [80] M. J. V. Streeter et al., Temporal feedback control of highintensity laser pulses to optimize ultrafast heating of atomic clusters, Appl. Phys. Lett. 112, 244101 (2018).
- [81] Z. H. He, B. Hou, V. Lebailly, J. A. Nees, K. Krushelnick, and A. G. R. Thomas, *Coherent control of plasma dynamics*, Nat. Commun. **6**, 7156 (2015).
- [82] T. D. Arber, K. Bennett, C. S. Brady, A. Lawrence-Douglas, M. G. Ramsay, N. J. Sircombe, P. Gillies, R. G. Evans, H. Schmitz, A. R. Bell, and C. P. Ridgers, Contemporary particle-in-cell approach to laser-plasma modelling, Plasma Phys. Controlled Fusion 57, 1 (2015).
- [83] D. Umstadter, J. K. Kim, and E. Dodd, Laser injection of ultrashort electron pulses into wakefield plasma waves, Phys. Rev. Lett. 76, 2073 (1996).
- [84] M. Chen, Z. M. Sheng, Y. Y. Ma, and J. Zhang, *Electron injection and trapping in a laser wakefield by field ionization to high-charge states of gases*, J. Appl. Phys. **99**, 1 (2006).
- [85] A. Pak, K. A. Marsh, S. F. Martins, W. Lu, W. B. Mori, and C. Joshi, *Injection and trapping of tunnel-ionized electrons* into laser-produced wakes, Phys. Rev. Lett. **104**, 025003 (2010).
- [86] C. McGuffey, A. G. R. Thomas, W. Schumaker, T. Matsuoka, V. Chvykov, F. J. Dollar, G. Kalintchenko, V. Yanovsky, A. Maksimchuk, K. Krushelnick, V. Y. Bychenkov, I. V. Glazyrin, and A. V. Karpeev, *Ionization induced trapping in a laser wakefield accelerator*, Phys. Rev. Lett. 104, 025004 (2010).
- [87] J. S. Liu, C. Q. Xia, W. T. Wang, H. Y. Lu, C. Wang, A. H. Deng, W. T. Li, H. Zhang, X. Y. Liang, Y. X. Leng, X. M. Lu, C. Wang, J. Z. Wang, K. Nakajima, R. X. Li, and Z. Z. Xu, All-optical cascaded laser wakefield accelerator using ionization-induced injection, Phys. Rev. Lett. 107, 035001 (2011).
- [88] B. B. Pollock et al., Demonstration of a narrow energy spread, ~0.5 GeV electron beam from a two-stage laser wakefield accelerator, Phys. Rev. Lett. **107**, 045001 (2011).
- [89] T. Matsuoka, C. McGuffey, P. G. Cummings, S. S. Bulanov, V. Chvykov, F. Dollar, Y. Horovitz, G. Kalintchenko, K. Krushelnick, P. Rousseau, A. G. R. Thomas, V. Yanovsky, and A. Maksimchuk, On electron betatron motion and electron injection in laser wakefield accelerators, Plasma Phys. Controlled Fusion 56, 084009 (2014).
- [90] I. Blumenfeld, C. E. Clayton, F.-J. Decker, M. J. Hogan, C. Huang, R. Ischebeck, R. Iverson, C. Joshi, T. Katsouleas, N. Kirby, W. Lu, K. A. Marsh, W. B. Mori, P. Muggli, E. Oz, R. H. Siemann, D. Walz, and M. Zhou, *Energy*

- doubling of 42 GeV electrons in a metre-scale plasma wakefield accelerator, Nature (London) 445, 741 (2007).
- [91] C. E. Clayton, E. Adli, J. Allen, W. An, C. I. Clarke, S. Corde, J. Frederico, S. Gessner, S. Z. Green, M. J. Hogan, C. Joshi, M. Litos, W. Lu, K. A. Marsh, W. B. Mori, N. Vafaei-Najafabadi, X. Xu, and V. Yakimenko, Self-mapping the longitudinal field structure of a nonlinear plasma accelerator cavity, Nat. Commun. 7, 12483 (2016).
- [92] K. Floettmann, *Some basic features of the beam emittance*, Phys. Rev. ST Accel. Beams **6**, 034202 (2003).
- [93] W. Lu, M. Tzoufras, C. Joshi, F. S. Tsung, W. B. Mori, J. Vieira, R. A. Fonseca, and L. O. Silva, Generating multi-GeV electron bunches using single stage laser wakefield acceleration in a 3D nonlinear regime, Phys. Rev. ST Accel. Beams 10, 061301 (2007).
- [94] S. Wilks, T. Katsouleas, J. M. Dawson, P. Chen, and J. J. Su, *Beam loading in plasma waves*, IEEE Trans. Plasma Sci. 15, 210 (1987).
- [95] M. Tzoufras, W. Lu, F. S. Tsung, C. Huang, W. B. Mori, T. Katsouleas, J. Vieira, R. A. Fonseca, and L. O. Silva, *Beam loading in the nonlinear regime of plasma-based acceleration*, Phys. Rev. Lett. 101, 145002 (2008).
- [96] J. P. Couperus, R. Pausch, A. Köhler, O. Zarini, J. M. Krämer, M. Garten, A. Huebl, R. Gebhardt, U. Helbig, S. Bock, K. Zeil, A. Debus, M. Bussmann, U. Schramm, and

- A. Irman, Demonstration of a beam loaded nanocoulombclass laser wakefield accelerator, Nat. Commun. **8**, 487 (2017).
- [97] G. G. Manahan, A. F. Habib, P. Scherkl, P. Delinikolas, A. Beaton, A. Knetsch, O. Karger, G. Wittig, T. Heinemann, Z. M. Sheng, J. R. Cary, D. L. Bruhwiler, J. B. Rosenzweig, and B. Hidding, Single-stage plasma-based correlated energy spread compensation for ultrahigh 6d brightness electron beams, Nat. Commun. 8, 15705 (2017).
- [98] J. Götzfried, A. Döpp, M. F. Gilljohann, F. M. Foerster, H. Ding, S. Schindler, G. Schilling, A. Buck, L. Veisz, and S. Karsch, *Physics of high-charge electron beams in laser-plasma wakefields*, Phys. Rev. X 10, 041015 (2020).
- [99] W. Lu, C. Huang, M. Zhou, M. Tzoufras, F. S. Tsung, W. B. Mori, and T. Katsouleas, *A nonlinear theory for multidimensional relativistic plasma wave wakefields*, Phys. Plasmas **13**, 056709 (2006).
- [100] T. Esirkepov, S. V. Bulanov, M. Yamagiwa, and T. Tajima, *Electron, positron, and photon wakefield acceleration: Trapping, wake overtaking, and ponderomotive acceleration*, Phys. Rev. Lett. **96**, 014803 (2006).
- [101] Z. Zhang, S. Zhou, and J. Liu, Transient chirp reconstruction of an ultrafast electron beam via a tightly focused chirped laser pulse, Opt. Lett. 50, 2025 (2025).